CZECH TECHNICAL UNIVERSITY IN PRAGUE

Faculty of Nuclear Sciences and Physical Engineering

Department of Physics

Dependence of Z boson kinematic variables on the parton distribution functions in the ATLAS experiment

Diploma thesis

Miroslav Myška

Supervisor: RNDr. Pavel Staroba, CSc., Institute of Physics,
Academy of Sciences of the Czech Republic, v.v.i., Prague

Academic year 2006/2007

Název práce:
Závislost kinematických proměnných Z bosonu na partonových distribučních funkcích v experimentu ATLAS

Autor: Miroslav Myška

Obor: Jaderné inženýrství

Druh práce: Diplomová práce

Vedoucí práce: RNDr. Pavel Staroba, CSc., FzÚ, AV ČR v.v.i.

Abstrakt: Cílem předkládané práce je kvantifikovat vliv neurčitosti znalostí partonových distribučních funkcí na kinematické veličiny Z bosonu vznikajícího v experimentu ATLAS. Zkoumaný rozpadový kanál je $Z \rightarrow e^+ + e^-$.

Teoretická část práce popisuje vývoj teorie strukturních funkcí protonu od elastického form faktoru až po partonové distribuční funkce i s jejich evolučními rovnicemi. Jedna kapitola je věnována popisu χ^2 testu a Kolmogorova-Smirnova testu tvaru rozdělení.

Generátorem Herwig/Jimmy bylo připraveno pět sad dat obsahujicích případy $pp \rightarrow X + Z \rightarrow e^- e^+$ lišící se pouze použitou partonovou distribuční funkcí. Pro testování podobností tvaru získaných rozdělení bylo použito Kolmogorova-Smirnova testu.

Klíčová slova: standardní model, kvantová chromodynamika, teorie elektroslabé interakce, strukturní funkce, partonové distribuční funkce, Z boson, experiment ATLAS .

Title:
Dependence of Z boson kinematic variables on the parton distribution functions in the ATLAS experiment

Author: Miroslav Myška

Specialization: Nuclear Engineering

Sort of project: Diploma thesis

Supervisor: RNDr. Pavel Staroba, CSc., IP, ASCR v.v.i.

Abstract: Main goal of this diploma thesis is to quantify the influence of uncertainty of our knowledge of parton distribution functions on the distribution of kinematic quantities of Z boson created in ATLAS experiment. The decay channel $Z \rightarrow e^+ + e^-$ is investigated.

The theoretical part of this work describes the theory of structure functions from elastic form factors to parton distribution functions and their evolution. Two most common statistical tests (χ^2 test and Kolmogorov-Smirnov test) used for comparison of shape of distributions are described in one chapter.

Five sets of data (differing only by parton distribution functions used) containing $pp \rightarrow X + Z \rightarrow e^- e^+$ events were generated by Herwig/Jimmy. Kolmogorov-Smirnov test was chosen as the most suitable for comparisons of shape of prepared distributions.

Keywords: Standard Model, quantum chromodynamics, theory of electroweak interaction, structure functions, parton distribution functions, Z boson, experiment ATLAS.

Prohlášení:

Prohlašuji, že jsem svou diplomovou práci vypracoval samostatně a použil jsem pouze podklady (literaturu, software, atd.) uvedené v přiloženém seznamu.

Nemám závažný duvod proti užití tohoto školního díla ve smyslu 60 Zákona č.121/2000 Sb., o právu autorském, o právech souvisejících s právem autorským a o změně něktrých zákonu (autorský zákon).

V Praze dne

Contents

Chapter 1

Introduction

Standard Model is very successful theory in description of physical phenomena observed in experiments performed up to now. ATLAS experiment at LHC will start to collect data in near future. A new kinematic area will be reached at full performance of the collider and theoretical predictions of Standard Model as well as other theories will be compared with data.

For the correct interpretation of measured data, it is necessary to investigate the influence of all possible sources of uncertainty: the theoretical one, uncertainty arising from detector effects and background. The aim of this work is to estimate the influence of the uncertainty of our knowledge of parton distribution functions of the proton on the distribution of kinematic quantities of the Z boson created in ATLAS experiment. The decay channel $Z \rightarrow e^+ + e^-$ is investigated.

There are many sets of parton distribution functions prepared by different physics collaborations. These parton distribution functions differ in valid kinematical area as well as in the order of global fit used for their extraction from data. Five sets of parton distribution functions widely used were chosen for this study.

The basic kinematic quantities characterizing deep inelastic scattering (DIS) and Drell-Yan lepton pair creation are described in Chapter 2. The formalism of lepton-hadron scattering based on structure functions is reported in Chapter 3. Parton model is introduced in Chapter 4. Structure functions are expressed in terms of parton distribution functions. The differential cross section of Z production in hadron-hadron collisions is discussed in Chapter 5. The most important experiments measuring proton structure functions are summarized in Chapter 6. Chapter 7 describes detector AT-

LAS and Chapter 8 summarizes a physical program planed to be performed at ATLAS. Chapter 9 shortly deals with the mechanism of generation of particle interactions with Monte Carlo generators Herwig [27] and Pythia [28]. Two most common statistical tests (χ^2 test and Kolmogorov-Smirnov test) used for comparison of distributions are described in Chapter 10.

The main part of this work (Chapter 11) is the analysis of events $pp \to X + Z \to e^- e^+$ generated by the above mentioned programs. Five sets of events (differing only by parton distribution functions used) were generated by Herwig. Two classes of comparisons are presented. The first one is the comparison of events generated by Herwig with different parton distribution functions. The second one is the comparison of distributions of kinematic quantities of the Z boson events generated with Herwig and Pythia. Kolmogorov-Smirnov test was chosen as the most suitable for these comparisons.

The natural unit system is applied in the whole study. Planck constant and speed of light is considered to be 1. The following conversion relations can be used to recompute the values of quantities in both directions:

$$1 \text{ kg} = 5.609589206\ 10^{26} \text{ GeV}$$
$$1 \text{ s} = 1.5192676\ 10^{24} \text{ GeV}^{-1}$$
$$1 \text{ m} = 5.06773122\ 10^{15} \text{ GeV}^{-1}.$$

Chapter 2

Kinematics

The main kinematic quantities characterizing deep inelastic scattering and Drell-Yan process will be defined in this chapter. The general formula for differential cross section will be shown. Particular cross sections will be discussed in following chapters.

The differential cross section for the process $1+2 \rightarrow 3+4+...n$ is given by equation [1]:

$$d\sigma = \frac{(2\pi)^4}{4\sqrt{(p_1.p_2)^2 - m_1^2.m_2^2}} \delta^4(\sum_{j=3}^{n} p_j - p_1 - p_2)|\mathcal{M}|^2 \prod_{i=3}^{n} \frac{d\vec{p_i}}{(2\pi)^3 2E_i}. \quad (2.1)$$

Matrix elements $\mathcal{M}$ describe processes between elementary particles and can be calculated in the framework of perturbative theory. Feynman developed method of calculation based on drawing of diagrams representing the interaction. Each part of diagram corresponds to given term and $\mathcal{M}$ is then given by their product. This method makes calculation of cross sections easier. The technique of Feynman diagrams enables in principle to calculate the invariant amplitude $\mathcal{M}$ in any order of the relevant coupling constant.

2.1 Deep inelastic scattering

The deep inelastic scattering is hard lepton-hadron collision. Only "neutral current" processes, when ingoing lepton is the same as outgoing, are assumed. These processes can be mediated by the exchange of either the photon or the

neutral vector boson Z. The latter contribution is dominant for really high energies. Let's consider electron-proton interaction.

The e-p scattering in the leading order is shown in Fig. 2.1. The fourmomentum of incoming electron is signed k and momentum of incoming proton of mass M is signed p. Fourmomentum of outgoing lepton is k'. The proton will often break up into complicated multi-particle states with large invariant mass W. If the final state of proton is described with fourmomentum P as a sum over all momenta of fragments, we will get $P^2 = W^2$. From momentum conservation follows $W^2 = (p+q)^2$. More detailed elements of proton structure can be resolved by increasing of the square of transferred momentum $q^2 = (k-k')^2$ of the photon. The transferred fourmomentum squared is negative in the relativistic approach: $q^2 < 0$. k^2 were neglected in relativistic limit.

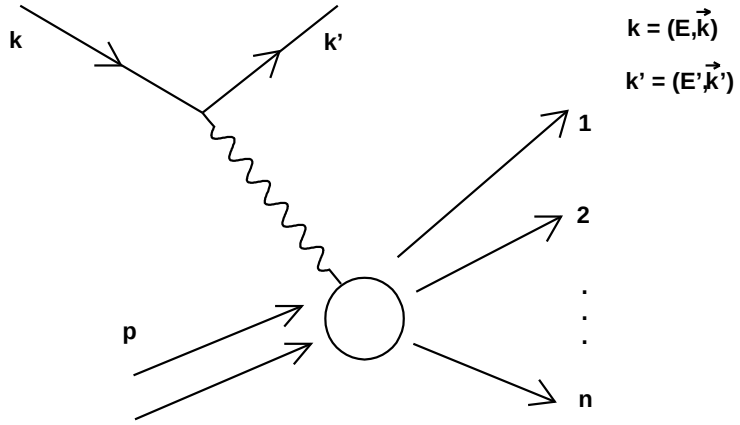

Figure 2.1: The lowest - order diagram for inclusive e-p deep inelastic scattering.

Two independent variables can describe the inelastic process. The following set of variables is commonly used [1]:

$$Q^2 = -q^2 = -(k-k')^2 = 2kk' = -2EE'(1-\cos\Theta) = 4EE'\sin^2(\Theta/2),$$
$$\nu = (p.q)/m = E - E', \tag{2.2}$$
$$x = Q^2/(2p.q) = Q^2/(2M\nu),$$
$$y = (p.q)/(p.k) = \nu/E.$$

The pairs $(\nu, q^2), (x, y)$ or (x, Q^2) are most often used to uniquely specify the state of the scattered electron and to write down the cross section provided that colliding particles are unpolarized.

It is possible to express other quantities in new variables. E.g. total CMS energy squared:

$$s = (k + p)^2 = M^2 + 2kp = M(2E + M) = M^2 + Q^2/(xy) \tag{2.3}$$

and invariant mass of the hadronic system:

$$W^2 = (p + q)^2 = Q^2(1 - x)/x + M^2 = 2M\nu - Q^2 + M^2. \tag{2.4}$$

All quantities defined above are relativistic invariant.

The term "deep inelastic scattering" means that both invariants Q^2 and pq are large with respect to M

$$Q^2 \gg M^2, \quad \nu \gg M.$$

The so called Bjorken limit corresponds to the case when $Q^2 \to \infty,\ pq \to \infty$ but the ratio x remains finite.

2.2 Drell-Yan process

Deep inelastic scattering is investigated by colliding electrons with a proton beam. Information about nucleon structure functions can be extracted from these experiments. Determination of the internal structure of other hadrons has to be performed by other method - collision of two hadrons as hard as possible. The process most similar to deep inelastic scattering is the annihilation of a quark and an antiquark, each deriving from a different hadron, into a lepton pair. This is called the Drell - Yan process [4]. The process is schematically shown in Fig. 2.2.

The invariant mass of the colliding protons with momenta P_a and P_b is

$$s = (P_a + P_b)^2. \tag{2.5}$$

Here a designates the first and b the second hadron.

Momenta of the partons participating in the Drell-Yan process can be expressed as

$$p_a = x_a\ P_a, \qquad p_b = x_b\ P_b. \tag{2.6}$$

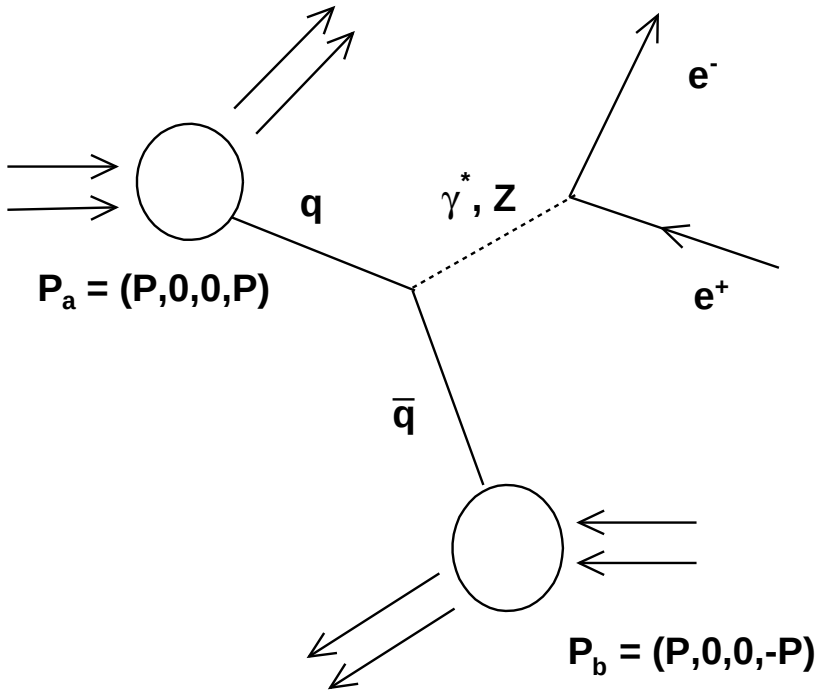

Figure 2.2: Schematic view of the Drell - Yan process in the p-p interaction.

x_a and x_b give the momentum fraction carrying by corresponding parton (quark). It means that $x_a, x_b \in (0, 1)$. Both quarks in Fig. 2.2 have to be of the same flavor and color.

The fourmomenta of outgoing leptons is equal to fourmomenta of vector boson and its square is

$$Q^2 = (p_a + p_b)^2. \tag{2.7}$$

Kinematic difference between Drell-Yan and deep inelastic scattering is that now is $Q^2 > 0$ in comparison with $q^2 =< 0$ for DIS. It is clear that $Q^2 = M^2$ holds with M the invariant mass of the leptonic pair. The running coupling constant still has its usual form with $\alpha(Q^2) \to \alpha(M^2)$.

Neglecting hadron and quark masses, the invariant mass of the lepton

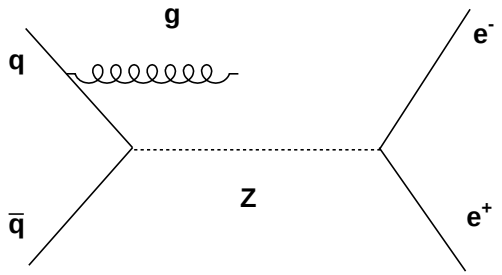

Figure 2.3: Drell - Yan process with Z in next to leading order.

pair is then

$$M^2 = (p_a + p_b)^2 = 2p_a\ p_b = 2x_a\ x_b\ P_a\ P_b = x_a\ x_b\ (P_a + P_b)^2 = x_a\ x_b\ s. \quad (2.8)$$

It is standard to express product of x_a and x_b from this equation and define new variable

$$\tau = x_a\ x_b = (M^2)/s. \quad (2.9)$$

The rapidity of the vector boson can be expressed as a function of fraction momenta of interacting partons as following:

$$y = \frac{1}{2} \ln\left(\frac{E + P_L}{E - P_L}\right) = \frac{1}{2} \ln\left(\frac{x_a}{x_b}\right), \quad (2.10)$$

where $P_L = x_a\ E_a - x_b\ E_b$.
It is possible to write the fractional momenta x_a and x_b using new variables as

$$x_a = e^y\ Q/\sqrt{s}, \quad x_b = e^{-y}\ Q/\sqrt{s}. \quad (2.11)$$

The head-on collision in leading order of two hadrons with zero transverse momentum was assumed. Consequently Z has the transverse momentum equal to zero. The non-zero p_t of the vector boson is generated by initial gluon radiation - see Fig. 2.3.

Chapter 3

Structure functions of the proton

3.1 Elastic scattering of electron on point-like proton

At the beginning of investigation of inner structure of proton it is necessary to find the cross section of elastic lepton-proton scattering for the case of point-like proton. This process is described in the lowest order of perturbative quantum electrodynamics by photon exchange diagram in Fig.3.1.

Using Feynman rules, the invariant amplitude is given by

$$\mathcal{M} = -e^2 \bar{u}(k', s_4)\gamma^\mu u(k, s_2)\frac{1}{q^2}\bar{u}(p', s_3)\gamma_\mu u(p, s_1). \tag{3.1}$$

To obtain the unpolarized cross section, the square of the matrix element $\mathcal{M}$ has to be summed over the spins s_3, s_4 of the final and averaged over the spins s_1, s_2 of the initial fermions [1]

$$\overline{|\mathcal{M}|^2} = \frac{8e^4}{q^4} 2M^2 E' E\Big(\cos^2\frac{\Theta}{2} - \frac{q^2}{2M^2}\sin^2\frac{\Theta}{2}\Big). \tag{3.2}$$

The first kinematic relation from 2.2 was used for the derivation of this formula. The final result 3.3 is reached by inserting 3.2 into 2.1, where the electron mass is neglected and dE' integration is performed.

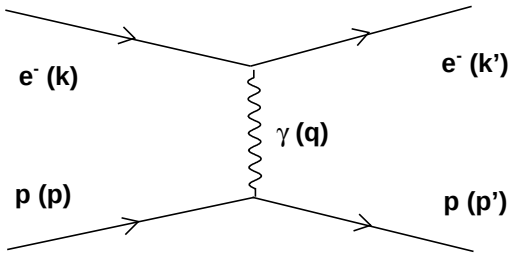

Figure 3.1: The LO diagram for e-p elastic scattering. The low energy photon interacts with the whole proton due to its large wavelength.

$$\frac{d\sigma}{d\Omega}\Big|_{lab} = \Big(\frac{\alpha^2}{4E^2 \sin^4 \frac{\Theta}{2}}\Big)\frac{E'}{E}\Big\{ \cos^2 \frac{\Theta}{2} - \frac{q^2}{2M^2} \sin^2 \frac{\Theta}{2}\Big\}. \tag{3.3}$$

Returning to 3.2, it is convenient to separate the sums over the electron and proton spins and to write $\overline{|\mathcal{M}|^2}$ as a contraction of two tensors

$$\overline{|\mathcal{M}|^2} = \frac{e^4}{q^4} L^{(e)\mu\nu} L^{(p)}_{\mu\nu}. \tag{3.4}$$

These tensors can be calculated by trace technique, which is described in many publications. Thus the tensor associated e.g. with the electron vertex is

$$L^{\mu\nu}_e = \frac{1}{2} \sum_{e \ spins} [\bar{u}(k')\gamma^\mu u(k)] \ [\bar{u}(k')\gamma^\nu u(k)]^*, \tag{3.5}$$

$$L^{\mu\nu}_e = \frac{1}{2} Tr\Big((\hat{k}' + m)\gamma^\mu(\hat{k} + m)\gamma^\nu\Big), \tag{3.6}$$

$$L^{\mu\nu}_e = 2(k'^\mu k^\nu + k'^\nu k^\mu - (k' \cdot k - m^2)q^{\mu\nu}). \tag{3.7}$$

This type of notation will be useful in next chapters for generalization from lepton tensor to hadron tensor.

3.2 Proton form factors

The above simplification can not be applied to the real structure of proton. Transition current for point spin-$\frac{1}{2}$ particle, which was assumed in previous section, is:

$$J^{\mu} = -e\bar{u}(k')\gamma^{\mu}u(k)e^{i(k'-k)\cdot x}. \tag{3.8}$$

This simple coupling has to be replaced with a structure, compatible with gauge and Lorentz invariance and parity conservation. The most general fourvector form can be constructed from p, p', q and the Dirac γ-matrices sandwiched between $\bar{u}$ and u. There are only two independent terms, γ^{μ} and $i\sigma^{\mu\nu}g_{\nu}$ that are functions of only one independent scalar variable q^2, where

$$\sigma^{\mu\nu} = \tfrac{i}{2}[\gamma^{\mu}\gamma^{\nu} - \gamma^{\nu}\gamma^{\mu}].$$

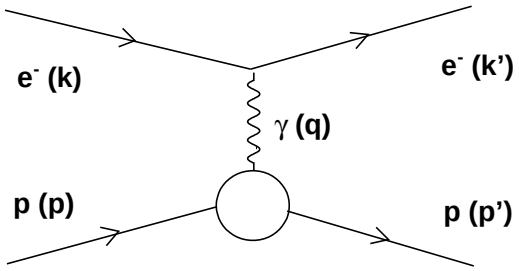

Figure 3.2: Electron proton elastic scattering. Structure of proton is described by elastic form factors dependent on q^2 (schematically represented by blob).

New transition current is connected with outer lines of proton in Fig. 3.2.

$$J^{\mu} = e\bar{u}(p')\Big[F_1(q^2)\gamma^{\mu} + \frac{\kappa}{2M}F_2(q^2)i\sigma^{\mu\nu}g_{\nu}\Big]u(p), \tag{3.9}$$

The $F_1(q^2)$ and $F_2(q^2)$ are two independent elastic electromagnetic form factors of the proton and parameterize our ignorance of the detailed structure of the proton. κ is anomalous magnetic moment. The proton is effectively seen as a particle of charge e and magnetic moment $(1+\kappa)e/2M$. κ of the proton is measured to be 1.793 [1]. In the case of point-like proton where

$q^2 \to 0$ is $\kappa = 0$ and the form factors of the proton must therefore be chosen so that

$$F_1(0) = 1, \qquad F_2(0) = 1.$$

The expression for differential cross section using 3.9 is

$$\frac{d\sigma}{d\Omega}\Big|_{lab} = \Big(\frac{\alpha^2}{4E^2 \sin^4 \frac{\Theta}{2}}\Big)\frac{E'}{E}\Big\{\Big(F_1^2 - \frac{\kappa^2 q^2}{4M^2}F_2^2\Big)\cos^2\frac{\Theta}{2} - \frac{q^2}{2M^2}(F_1+\kappa F_2)^2 \sin^2\frac{\Theta}{2}\Big\}, \tag{3.10}$$

This result was derived first by Rosenbluth in 1950 and therefore this formula bears his name.

Instead of F_1 and F_2, it is convenient to introduce their special linear combinations G_E and G_M, called electric and magnetic form factors

$$G_E = F_1 + \frac{\kappa q^2}{4M^2}F_2, \tag{3.11}$$

$$G_M = F_1 + \kappa F_2. \tag{3.12}$$

They are defined so that no interference terms occur in the calculation of the cross section. With definition $\tau = \frac{-q^2}{4M^2}$ equation 3.10 becomes

$$\frac{d\sigma}{d\Omega}\Big|_{lab} = \Big(\frac{\alpha^2}{4E^2 \sin^4 \frac{\Theta}{2}}\Big)\frac{E'}{E}\Big(\frac{G_E^2 + \tau G_M^2}{1+\tau}\cos^2\frac{\Theta}{2} + 2\tau G_M^2 \sin^2\frac{\theta}{2}\Big). \tag{3.13}$$

3.3 Inelastic electron-proton scattering

Inelastic interactions in Fig. 2.1, where the proton is recoiled into many final states, can not be described only by construction of general form of proton current J^μ. The expression for the invariant amplitude is directly generalized from form 3.4 to

$$\overline{|\mathcal{M}|^2} = \frac{e^4}{q^4}L^{\mu\nu}W_{\mu\nu}, \tag{3.14}$$

where $L^{\mu\nu}$ represents the lepton tensor of 3.5 and $W_{\mu\nu}$ is hadronic tensor. Its most general form must be constructed out of the independent momenta p and q, symmetric metric tensor $g^{\mu\nu}$, and totally antisymetric Levi-Civita pseudotensor $\epsilon_{\mu\nu\alpha\beta}$ [4]

$$W_{\mu\nu}(p,q) = -W_1 g_{\mu\nu} + W_2 \frac{p_\mu p_\nu}{M^2} + iW_3 \epsilon_{\mu\nu\alpha\beta} p_\alpha q_\beta$$

$$+ W_4 q_\mu q_\nu + W_5 (p_\mu q_\nu + p_\nu q_\mu) + iW_6 (p_\mu q_\nu - p_\nu q_\mu). \tag{3.15}$$

In the above decomposition $W_i(p,q)$ are unknown functions of p and q, which depend on the internal structure of the proton. But only three of them are, however, independent. Antisymmetric term vanish by $W_3(p,q) = 0$ when the parity conservation is true. Gauge invariance, expressed as the condition:

$$q^\mu W_{\mu\nu} = [-W_1 + W_4 q^2 + W_5 (pq)] q_\nu + [W_2 \frac{pq}{M^2} + W_5 q^2] p_\nu + iW_6 [(pq) q_\nu - q^2 p_\nu] = 0, \tag{3.16}$$

leads to three relations:

$$W_6(p,q) = 0, \tag{3.17}$$

$$W_5(p,q) = -W_2(p,q) \frac{pq}{q^2 M^2}, \tag{3.18}$$

$$W_4(p,q) = W_1(p,q) \frac{1}{q^2} + W_2(p,q) \frac{(pq)^2}{q^4 M^2}. \tag{3.19}$$

This simplifies 3.15 to [1]

$$W_{\mu\nu}(p,q) = -W_1(p,q) \Big(g_{\mu\nu} - \frac{q_\mu q_\nu}{q^2} \Big) + \frac{W_2(p,q)}{M^2} \Big(p_\mu - \frac{pq}{q^2} q_\mu \Big) \Big(p_\nu - \frac{pq}{q^2} q_\nu \Big). \tag{3.20}$$

The additional term in hadronic tensor will appear in cases of non-conservation of P-parity, [13]:

$$W_{\mu\nu}(p,q) = \ldots - \frac{W_3(p,q)}{M^2} \Big(i \epsilon_{\mu\nu\alpha\beta} p^\alpha q^\beta \Big). \tag{3.21}$$

Invariant amplitude for $ep \to eX$ is

$$\overline{|\mathcal{M}|^2} = \frac{e^4}{q^4} 4W_1 (k.k') + \frac{2W_2}{M^2} [2(p.k)(p.k') - M^2 k.k']. \tag{3.22}$$

Instead of W_1 and W_2 it is common to introduce another pair of functions

$$F_1 = M\ W_1, \qquad F_2 = \nu\ W_2. \tag{3.23}$$

The double differential cross sections written in two equivalent ways differing in the choice of pair of variables are

$$\frac{d\sigma}{dE'd\Omega}\Big|_{lab} = \frac{\alpha^2}{4E^2\sin^4\frac{\Theta}{2}}\Big[W_2(\nu,q^2)\cos^2\frac{\Theta}{2} + 2W_1(\nu,q^2)\sin^2\frac{\Theta}{2}\Big], \qquad (3.24)$$

$$\frac{d\sigma}{dxdQ2} = \frac{4\pi\alpha^2}{Q^4}\Big[\Big(1-y-\frac{M^2xy}{s}\Big)\frac{F_2(x,Q^2)}{x} + \frac{1}{2}y^2 2F_1(x,Q^2)\Big]. \qquad (3.25)$$

The unknown functions $F_i(x,Q^2)$ are called inelastic electromagnetic form factors or structure functions of the proton.

These cross sections were calculated for the case of the exchange of unpolarized virtual photon. Now it is possible to transfer the problem on scattering by a real photon with energy ν and polarization ϵ off the unpolarized proton. The total cross section for photon with helicity λ is

$$\sigma_\lambda^{tot} = \frac{4\pi^2\alpha}{K}\epsilon_\lambda^{\mu *}\epsilon_\lambda^{\nu}W_{\mu\nu}. \qquad (3.26)$$

Using expression 3.15 for $W_{\mu\nu}$, the transverse and longitudinal cross sections are

$$\sigma_T = \frac{4\pi^2\alpha}{K}W_1(\nu,q^2), \qquad (3.27)$$

$$\sigma_L = \frac{4\pi^2\alpha}{K}\Big[\Big(1-\frac{\nu^2}{q^2}\Big)W_2(\nu,q^2) - W_1(\nu,q^2)\Big], \qquad (3.28)$$

where K satisfies

$$K = \frac{W^2-M^2}{2M} = \nu + \frac{q^2}{2M}. \qquad (3.29)$$

Chapter 4

Parton distribution functions

4.1 Basic ideas of parton model

The parton model develops an experimental fact, that such complex system like proton starts for really small wavelengths (large Q^2) of virtual photons to behave like a group of free Dirac particles, see Fig. 4.1.

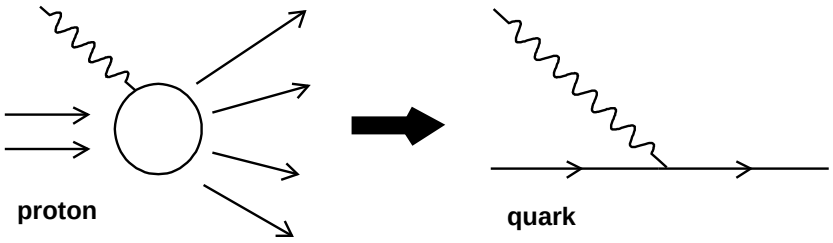

Figure 4.1: The electromagnetic interaction between electron and proton behaves for sufficiently small wavelengths of virtual photons like coupling a photon with point-like charge - charged parton.

The structure functions for inelastic electron-proton scattering (3.24) become at large Q^2 [1]

$$2W_1 = \frac{Q^2}{2m^2}\delta(\nu - \frac{Q^2}{2m}),$$
$$W_2 = \delta(\nu - \frac{Q^2}{2m}), \tag{4.1}$$

or equivalently:

$$2mW_1(\nu, Q^2) = \frac{Q^2}{2m\nu}\delta(1 - \frac{Q^2}{2m\nu}),$$

$$\nu W_2(\nu, Q^2) = \delta(1 - \frac{Q^2}{2m\nu}). \tag{4.2}$$

Generally, an inelastic electron-proton scattering at large Q^2 is viewed simply as elastic scattering of electron on "free" quark within the proton. These structure functions are often called "point" functions.

"Point" functions display intriguing property, that they are only functions of dimensionless ratio

$$\omega = \frac{2M\nu}{Q^2} \tag{4.3}$$

and not of Q^2 and ν independently. This property, that structure functions are independent of Q^2 at constant ω, is called Bjorken scaling.

The parton model describes the proton as a composition of many "point" partons (quarks and gluons), each carrying a different fraction x of the parent proton momentum and energy. Both the proton and its parton move along the z axis, therefore the longitudinal and transverse momenta are

	proton	**parton**
energy	E	xE
momenta	p_L = p	p_L = xp
	$p_T = 0$	$p_T = 0$
mass	M	xM

The parton (momentum) distribution functions

$$f_i(x) = \frac{dP_i}{dx} \tag{4.4}$$

describe the probability that the struck parton i carries a fraction x of the proton momentum p. The sum over all partons (charged as well as not charged) has to create the whole proton, therefore

$$\sum_j \int dx\ x\ f_j(x) = 1. \tag{4.5}$$

It is common to redefine a structure functions for parton with momentum fraction x:

$$xmW_1(\nu, Q^2) \to F_1(\omega) \to F_1(x), \tag{4.6}$$

$$\nu W_2(\nu, Q^2) \to F_2(\omega) \to F_2(x). \tag{4.7}$$

In addition to F_1 and F_2 it is useful to introduce the so called longitudinal structure function

$$F_L(x, Q^2) = F_2(x, Q^2)\Big(1 + \frac{4M^2x^2}{Q^2}\Big) - 2xF_1(x, Q^2). \tag{4.8}$$

The ratio of longitudinal and transversal cross section is:

$$R(x, Q^2) = \frac{\sigma_L(x, Q^2)}{\sigma_T(x, Q^2)} = \frac{F_L(x, Q^2)}{2xF_1(x, Q^2)}. \tag{4.9}$$

Summing results for F_1 and F_2 for fraction x over the partons making up a proton, it is obtained

$$F_2(x) = \sum_i e_i^2 x f_i(x), \tag{4.10}$$

$$F_1(x) = \frac{1}{2x} F_2(x). \tag{4.11}$$

The second formulae is known as the Callan-Gross relation. i sums only over the charged partons, which can interact with a photon. Using this basic idea of parton model, the cross section can be expressed as follows[1]

$$\frac{d\sigma}{dxdy}\Big|_{ep\to eX} = \frac{2\pi\alpha^2}{Q^4} s\Big[1 + (1-y)^2\Big] \sum_i e_i^2 x f_i(x), \tag{4.12}$$

where the particle masses are neglected.

Identity 4.10 can be made more concrete by including terms from additive quark model:

$$\frac{1}{x}F_2(x) = \left(\frac{2}{3}\right)^2 [u(x) + \bar{u}(x)] + \left(\frac{1}{3}\right)^2 [d(x) + \bar{d}(x)] + \left(\frac{1}{3}\right)^2 [s(x) + \bar{s}(x)] \ \ldots \tag{4.13}$$

where $u(x)$ and $\bar{u}(x)$ are the probability distributions of u quarks and antiquarks within the proton, $d(x)$ and $\bar{d}(x)$ are the probability distributions of d quarks and antiquarks atc.

4.2 Higher orders of deep inelastic e-p scattering

The parton model in previous section completely ignores the dynamical role of neutral partons. In quark model, these constituents are gluons, carriers of the strong force. Quark may radiate a gluon before or after being struck by the virtual photon. This process $\gamma^* q \to qg$ is shown in Fig. 4.2.

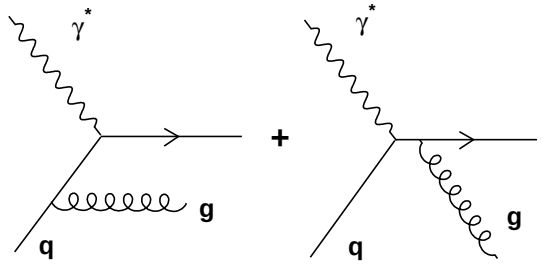

Figure 4.2: Initial- or final-state gluon radiation contributes to inclusive e-p deep inelastic scattering in O($\alpha\alpha_s$).

Moreover, a gluon participated in the proton structure can contribute to deep inelastic scattering via $\gamma^* g \to q\bar{q}$. Fig. 4.3 shows such $q\bar{q}$ pair creation. Despite of the leading order of DIS $O(\alpha)$, these processes are $O(\alpha\alpha_s)$ contributions to the cross section. The emission of gluon has two experimentally observable consequences. First, the scaling property of the structure functions will no longer be true and second, the outgoing quark will no longer be collinear with the virtual photon. These produced jets Will gain a nonzero transverse momentum p_T relative to the virtual photon.

The results for QED process $\gamma^* e \to \gamma e$ can be used for the calculation of invariant amplitude for process $\gamma^* q \to qg$. It can be written using substitution $\alpha^2 \to e_i^2 \alpha\alpha_s$ as

$$\overline{|M|^2} = 32(e_i^2\alpha\alpha_s)\frac{4}{3}\Big(-\frac{t}{s}-\frac{s}{t}+\frac{2uQ^2}{st}\Big), \tag{4.14}$$

where the factor 4/3 takes into account the summation over final and averaging over initial colours. The square of the transverse momentum of

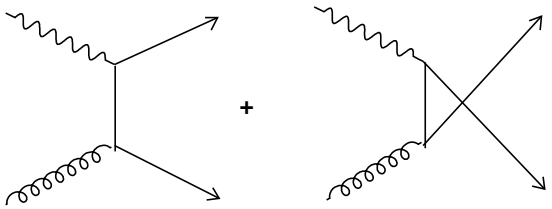

Figure 4.3: The gluon - initiated scattering contributions to inclusive e-p DIS in $O(\alpha\alpha_s)$.

the outgoing quark, $p_T = k' \sin\Theta$, can be expressed in the limit of small-angle scattering (-t $\ll$ s) as

$$p_T^2 = \frac{s(-t)}{s+Q^2} \tag{4.15}$$

and the solid angle differential is then

$$d\Omega = \frac{4\pi}{s} dp_T^2. \tag{4.16}$$

Using (4.15) and definition of momentum fraction z:

$$z = \frac{Q^2}{2p_i q}, \tag{4.17}$$

based on kinematics in Fig. 4.4, the cross section becomes [1]

$$\frac{d\sigma}{dp_T^2} = e_i^2 \sigma_0 \frac{1}{p_T^2} \frac{\alpha_s}{2\pi} P_{qq}(z), \tag{4.18}$$

where $\sigma_0 = 4\pi^2\alpha_s$ and

$$P_{qq}(z) = \frac{4}{3}\Big(\frac{1+z^2}{1-z}\Big) \tag{4.19}$$

represents the probability of gluon emission from quark and so becoming a quark with momentum reduced by a fraction $z = x/y$.

At high energy (s large), hence in the region -$t \ll s$, the cross section (4.18) represents the full p_T^2 distribution of the final-state parton jets. If calculated

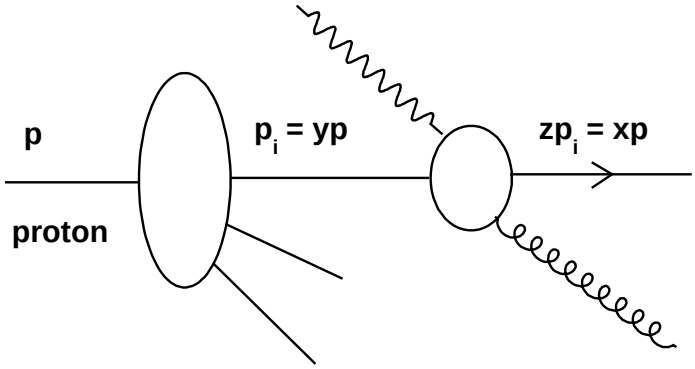

Figure 4.4: Schematic illustration of photon - parton interaction with gluon in final-state. The initial parton momentum fraction is y and final momentum fraction of that parton is x.

$$\sigma(\gamma^* q \to qg) = \int_{\mu^2}^{s/4} dp_T^2 \frac{d\sigma}{dp_T^2} \cong e_i^2 \sigma_0 \int_{\mu^2}^{s/4} \frac{dp_T^2}{p_T^2} \frac{\alpha_s}{2\pi} P_{qq}(z)$$

$$\cong e_i^2 \sigma_0 \Big(\frac{\alpha_s}{2\pi} P_{qq}(z) \log \frac{Q^2}{\mu^2} \Big), \tag{4.20}$$

it is clearly seen, that Bjorken scaling is violated due to the presence of the $\log Q^2$ factor. The structure function is directly modified to

$$\frac{F_2(x,Q^2)}{x} = \sum_q e_q^2 \int_x^1 \frac{dy}{y} q(y) \Big(\delta\Big(1 - \frac{x}{y}\Big) + \frac{\alpha_s}{2\pi} P_{qq}\Big(\frac{x}{y}\Big) \log \frac{Q^2}{\mu^2} \Big), \tag{4.21}$$

where the notation for quark structure function $q(y) = f_q(y)$ have been introduced. The maximum p_T of the gluon

$$\Big(p_T^2\Big)_{max} = \frac{s}{4} = Q^2 \frac{1-z}{4z} \tag{4.22}$$

was used in derivation of (4.20). The lower limit was set as μ in order to regularize the divergence when $p_T^2 \to 0$.

It seems very useful to absorb the $\log Q^2$ term in (4.21) into a modified quark probability distribution

$$\frac{F_2(x,Q^2)}{x} = \sum_q e_q^2 \Big(q(x) + \Delta q(x,Q^2) \Big), \tag{4.23}$$

where

$$\Delta q(x,Q^2) = \frac{\alpha_s}{2\pi} \log\Big(\frac{Q^2}{\mu^2}\Big) \int_x^1 \frac{dy}{y} q(y) P_{qq}\Big(\frac{x}{y}\Big). \tag{4.24}$$

The quark densities $q(x,Q^2)$ now depend on Q^2. By the Q^2 evolution of the quark densities it is meant an integro-diferencial equation for $q(x,Q^2)$:

$$\frac{d}{d\log Q^2} q(x,q^2) = \frac{\alpha_s}{2\pi} \int_x^1 \frac{dy}{y} q(y,Q^2) P_{qq}\Big(\frac{x}{y}\Big). \tag{4.25}$$

Now the $O(\alpha\alpha_s)$ process described in Fig. 4.3 has to be incorporated into $ep \to eX$. Similarly as for the first process, the QED Compton scattering invariant amplitude is used for calculation

$$\overline{|M|^2} = 32\pi^2 (e_q^2 \alpha\alpha_s) \frac{1}{2} \Big(\frac{u}{t} + \frac{t}{u} - \frac{2sQ^2}{tu} \Big). \tag{4.26}$$

Hence, the proton structure function contains the additional contribution

$$\frac{F_2(x,Q^2)}{x} = \ldots + \sum_q e_q^2 \int_x^1 \frac{dy}{y} g(y) \frac{\alpha_s}{2\pi} P_{qg}\Big(\frac{x}{y}\Big) \log\frac{Q^2}{\mu^2} \tag{4.27}$$

Here $g(y)$ is the gluon density in the proton and

$$P_{qg} = \frac{1}{2}\Big(z^2 + (1-z)^2 \Big) \tag{4.28}$$

represents the probability, that a gluon annihilates into a $q\bar{q}$ pair. This newly created quark has a fraction momentum z. The quark evolution equation becomes

$$\frac{dq_i(x,Q^2)}{d\log Q^2} = \frac{\alpha_s}{2\pi} \int_x^1 \frac{dy}{y} \Big(q_i(y,Q^2) P_{qq}\Big(\frac{x}{y}\Big) + g(y,Q^2) P_{qg}\Big(\frac{x}{y}\Big) \Big) \tag{4.29}$$

for each quark flavor i.

Gluon evolution equation can be derived by applying of analogous arguments for quarks. It has a form

$$\frac{dg(x,Q^2)}{d\log Q^2} = \frac{\alpha_s}{2\pi}\int_x^1 \frac{dy}{y}\Big(\sum_i q_i(y,Q^2)P_{gq}\Big(\frac{x}{y}\Big) + g(y,Q^2)P_{gg}\Big(\frac{x}{y}\Big)\Big), \quad (4.30)$$

where the sum runs over quarks and antiquarks of all flavors. Equations (4.29) and (4.30) are known as DGLAP (Dokshitzer-Gribov-Lipatov-Altareli-Parisi) equations. Probability functions (corresponding to Feynman diagrams as in Fig. 4.5) are

$$P_{gq}(z) = \frac{4}{3}\frac{1+(1-z)^2}{z}, \quad (4.31)$$

$$P_{gg}(z) = 6\Big(\frac{1-z}{z} + \frac{z}{1-z} + z(1-z)\Big). \quad (4.32)$$

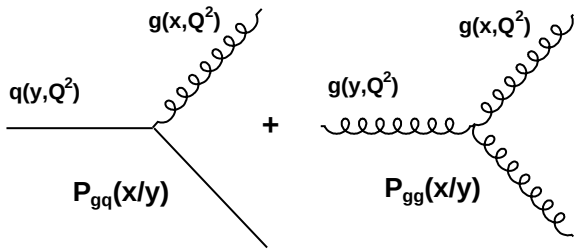

Figure 4.5: Feynman diagrams representing gluon vertices embedded in gluon structure functions.

Other $O(\alpha\alpha_s)$ contributions designed in Fig. 4.6 are of the form $\delta(1-z)$ and are singular at $z=1$. They must be such, that the total probability $P_{qq}(z)$ satisfies the constraint

$$\int_0^1 P_{qq}(z)dz = 0 \quad (4.33)$$

This modification of $P_{qq}(z)$ can be conveniently expressed in terms of the so-called "+ prescription" formalism. Here the term $1/(1-z)$ is replaced by $1/(1-z)_+$ due to regularization. The "+ prescription" is defined as

$$\int_0^1 dz\frac{f(z)}{(1-z)_+} = \int_0^1 dz\frac{f(z)-f(1)}{1-z}, \quad (4.34)$$

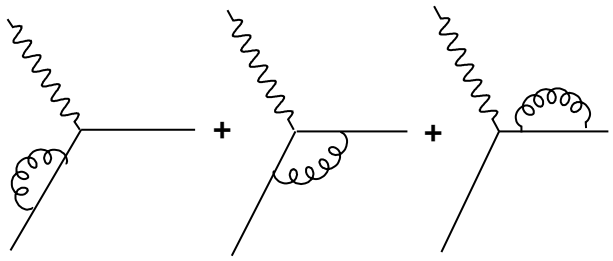

Figure 4.6: Three types of virtual gluon diagrams.

where $(1-z)_+ = (1-z)$ for $z < 1$ but is infinite at $z = 1$.

These P functions are summarily called the splitting functions and are given by perturbative expansions, beginning with $O(\alpha_s)$ [32]:

$$P_{ab}(z, \alpha_s(Q^2)) = P_{ab}^{(1)}(z)\frac{\alpha_s(Q^2)}{\pi} + P_{ab}^{(2)}(z)\frac{\alpha_s(Q^2)}{\pi}^2 + \dots . \tag{4.35}$$

The leading order splitting functions are [12]

$$P_{qq}(z) = \frac{4}{3}\Big[\frac{1+z^2}{1-z}\Big]_+ = \frac{4}{3}\Big[\frac{1+z^2}{(1-z)_+}\Big] + 2\delta(1-z), \tag{4.36}$$

$$P_{qg}(z) = \frac{1}{2}\Big[z^2 + (1-z)^2\Big], \tag{4.37}$$

$$P_{gq}(z) = \frac{4}{3}\Big[\frac{1+(1-z)^2}{z}\Big], \tag{4.38}$$

$$P_{gg}(z) = 6\Big[\frac{1-z}{z} + z(1-z) + \frac{z}{(1-z)_+}\Big] + \Big[\frac{11}{2} - \frac{n_f}{3}\Big]\delta(1-z), \tag{4.39}$$

where n_f is the number of (active) quark flavors.

4.3 Determination of the parton distributions from experiments

As was mentioned above for the solution of the evolution equations, the parton distributions are related to experimental results. The technique of

the evaluation of parton densities from experimental data is called "global analysis" or "global fitting", respectively.

Two major physics groups provide such global fits to existing data: CTEQ and MRST collaborations. In addition, there are also PDFs available from Alekhin and from two HERA experiments. The main source of the information on quark distributions is the measurement of deep inelastic scattering structure function (F_2, F_3) and of lepton pair creation cross section (e.g. Drell-Yan). The gluon distribution function figures directly in jet production processes.

The idea of the global fitting is to adjust the parton distributions to make theory and experiment agree. The theoretical analysis of the examined process has to be carried out at a specific order (LO, NLO, ...) and in a specific renormalization and factorization scheme ($\overline{MS}$ scheme, DIS scheme, fixed flavor scheme, ...).

The input parton distributions to the theoretical calculations are gained as follows. The parton distributions are written in terms of several parameters at chosen starting scale Q_0. The reference value Q_0 is usually chosen in the range $(1-2)GeV$ [33]. The parametrization must be general enough to accommodate all possible x and quark flavor dependence, but it should not contain so many parameters that the fitting procedure becomes very much underdetermined. All global analyses use a generic form for the parametrization of both the quark and gluon distributions [13]:

$$f(x, Q_0) = A_0 x^{A_1} (1-x)^{A_2} P(x; A_3, \ldots). \tag{4.40}$$

In the above expression , x^{A_1} dominates the small-x feature and $(1-x)^{A_2}$ determines the large-x behavior. The term $P(x; A_3, \ldots)$ is a suitably chosen smooth function, depending on one or more parameters, that adds more flexibility to the PDF parametrization. For example, one may choose [31]

$$P(x; A_3, A_4) = (1 + A_4 x)^{A_5}. \tag{4.41}$$

The parameterizations are chosen so that the flavor sum rule

$$\int_0^1 dx \Big[f_{u/p}(x, Q^2) - f_{\bar{u}/p}(x, Q^2) \Big] = 2 \tag{4.42}$$

and momentum sum rule

$$\sum_a \int_0^1 dx x f_{a/p}(x, Q^2) = 1 \tag{4.43}$$

are obey exactly [31]. These sum rules follow from the operator definitions of PDF. These equations determine $f_{a/p}(x, Q_0)$ from which $f_{a/p}(x, Q^2)$ for all Q^2 can be calculated using the evolution equations.

The extraction of $f_{a/p}(x, Q^2)$ has been described. The theoretical calculations can be now finished and compare with the data. This sequence is iterated, adjusting the parameters to get a best fit.

Chapter 5

Z boson production in hadron-hadron collisions

Calculation of the Drell-Yan hard scattering cross section in hadron-hadron collisions using factorization theorem will be discussed in this chapter. Kinematics of the Drell-Yan process is described in Chapter 2. It was first pointed out by Drell and Yan [34] more than 30 years ago that parton model ideas developed for deep inelastic scattering could be extended to certain processes in hadron-hadron collisions.

It was postulated that the hadronic cross section $\sigma(pp \to e^+e^- + X)$ could be in LO obtained by factorization of the subprocess cross section $\hat{\sigma}$ for $q\bar{q} \to e^+e^-$ by the proton distribution functions [33]:

$$\sigma_{DY} = \sum_{ab=q\bar{q},\bar{q}q} \int dx_a dx_b f_{a/A}(x_a) f_{b/B}(x_b) \hat{\sigma}_{ab\to X}, \tag{5.1}$$

Problems, however, appeared to arise when perturbative corrections from real and virtual gluon emission were calculated. Large logarithms from gluons emitted collinear with the incoming quarks appeared to spoil the convergence of the perturbative expansion. These logarithms were the same as those that arose in derivation of PDF evolution (4.24) and can therefore be absorbed in the definition of the parton distributions. Taking into account the leading logarithm corrections, (5.1) becomes [5]

$$d\sigma_{DY} = \Big[f_a(x_a, Q^2) \cdot \bar{f}_b(x_b, Q^2) + \bar{f}_a(x_a, Q^2) \cdot f_b(x_b, Q^2) \Big] \times \sigma^{Born}(q\bar{q} \to Z) dx_a dx_b. \tag{5.2}$$

σ^{Born} is cross section for annihilation of a pair quark and antiquark of invariant mass Q into a vector boson Z at the Born level. This cross section is calculated to be [33]

$$\hat{\sigma}^{q\bar{q}\to Z} = \frac{\pi}{3}\sqrt{2}G_F M_Z^2(v_q^2 + a_q^2)\delta(\hat{s} - M_Z^2), \tag{5.3}$$

where v_q (a_q) is the vector (axial vector) coupling of the Z to the quarks. This formula is valid in the narrow width production in which the decay width of the gauge boson is neglected.

When the σ_{DY} was measured, it turned out that the experimental cross section exceed the prediction by a factor of about 2. This factor is termed the "K factor" [5]. To gain a deeper understanding of the problems in Drell-Yan reactions, it is essential to incorporate first-order gluon corrections to the annihilation graph $q\bar{q} \to Z$, see Fig. 2.3. These gluon radiations from the initial state then generate the nonzero $p_T = Q_T$ of the Z boson. One can continue by pursing this tedious calculation order by order, but the problem of the perturbation theory is, that the cross section $d\sigma/dQ^2dQ_T^2$ contains a term proportional to $\ln^{2n}(Q^2/Q_T^2)$ and in $Q_T \ll Q$ region diverge at every fixed power n of the α_s [14].

These large logarithms can be removed by the resummation technique. This idea is based on possibility to iterate some types of corrections into geometric or exponential series and then summed up them. The standard procedure of resummation is leading-logarithm approximation(LLA), connected with definition of Sudakov form factor $S(\Theta)$ [5]. This function express the probability that after n-gluon emissions the outgoing quark still has a scattering angle $p_T/p_{||} < \Theta$, with p_T and $p_{||}$ being defined with respect to the original quark momentum.

Similar method of resummation for the Drell-Yan production was used first by Dokshitzer, Diakonov and Troyan [15]. They showed in Q_T space, that dominant contributions in the region of small Q_T can be resummed into a Sudakov form factor by double leading-logarithm approximation(DLLA). The disadvantage of this method is, that some subleading logarithms can be resummed only in the b-space, which is a Fourier conjugate of the Q_T space. b is called impact parameter. The b-space resummation method was introduced by Parisi and Petronzio [16]

In the framework of improved b-space resummation, Collins, Soper and Sterman derived a formalism for the transverse momentum distributions of vector boson production in hadronic collisions [17]. This formalism is often

called the CSS formalism.

Chapter 6

Experiments

6.1 Electron scattering with static proton target

Up to now only several experiments aimed measuring the structure functions of proton. This challenging task can be performed only in the greatest accelerating centers in the world, which can produce high energy collisions and have a precision detection apparatus at disposal. For this purpose leptons were soon recognized as the best probes of protons because of their well-understood electromagnetic interactions.

The first e-p scattering experiments investigating the structure of nucleons were performed by a group led by Robert Hofstadter at Stanford University from 1955. These investigations with static proton target and electron beam of energies from 200 MeV up to 1 GeV earned Hofstadter the Nobel prize for physics in 1961 [4].

In 1967, new electron linear accelerator was built in Stanford Linear Accelerator Center (SLAC) with electron beam energy up to 20 GeV. The first serious study of deep inelastic e-p scattering was started by the group of experimentalists from SLAC and MIT (Massachusetts Institute of Technology). They discovered that proton contains tiny scattering centres. This was the first evidence of point-like charged structures in the proton and support for newly formulated quark model. A new type of physics was opened up: DIS. These first MIT-SLAC results attracted the attention of Feynman who developed the basic ideas of the parton model (1968).

After that, physicists tried to probe deeper and deeper into depths of the

proton. Generally, the extraction of the structure functions was based on the measurements of double differential cross section $d\sigma/dxdQ^2$ of deep inelastic lepton-hadron scattering. Each experiment has its own kinematic range of Bjorken variable x and transferred momentum squared Q^2 (as shown in Fig. 6.1) as well as the type of probing lepton. Main experiments are summarized in Table 6.1.

A series of eight other experiments at SLAC collected data during the years 1970 and 1985. They provided detailed knowledge of deep inelastic e-p scattering cross section. Structure functions $F_2(x, Q^2)$ and the radio $R(x, Q^2)$ were determined by the fitting procedure for all precise measurements over the entire SLAC kinematic range $0.06 \leq \mathrm{x} \leq 0.9$ and $0.6 \leq Q^2 \leq 30.0$ (GeV)^2 [20].

6.2 Muon scattering with static proton target

In the next stage of proton structure investigation, more energetic lepton beams were necessary. It was difficult to produce such high-energy electron beams because of their energy losses through synchrotron radiation. Thus, muons became a natural choice as high-energy massive lepton probes with sufficient lifetime. In the following experiments, the muon beam was a tertiary beam obtained from the decay of charged pions and kaons, which in turn were obtained from the interaction of primary protons.

In the European Centre of Nuclear Research (CERN), several experiments were running in 1978-1985 under BCDMS (Bologna-CERN-Dubna-Munich-Saclay) Collaboration [30] and New Muon Collaboration (NMC) in 1986 - 1989. Data for these measurements of the proton structure function F_2 and the ratio R were collected at CERN SPS with static liquid-hydrogen target and muon beam with the highest energy of 280 GeV. BCDMC Collaboration provided a high statistics measurements with high Q^2 (7 - 260 (GeV)^2) and covered range of Bjorken variable $0.06 \leq \mathrm{x} \leq 0.8$. Analysis of the structure function was based on 1.81 10^6 reconstructed events after all cuts [21]. NMC measured inclusive deep inelastic μ-p cross sections in the kinematic range $0.002 \leq \mathrm{x} \leq 0.6$ and $0.5 \leq Q^2 \leq 75$ (GeV)^2. The ratio of the longitudinally and transversally polarized virtual photon absorption cross section, R, was measured for $0.002 \leq \mathrm{x} \leq 0.120$ and $1.0 \leq Q^2 \leq 25$ (GeV)^2. The full NMC

data set consists of 0.54 10^6 events from the small angle trigger and 1.82 10^6 events from the large angle trigger [23].

The aim of another experiment signed Experiment 665 at Fermi National Laboratory in Batavia was to measure proton structure function $F_2(x, Q^2)$ in fixed-target inelastic muon scattering. Data were taken during the years 1987 - 1992 excluding 1989 when the detector was being upgraded. Total number of events was 159 853. The highest energy of muon beam was 470 GeV and these are the first precise measurements of $F_2(x, Q^2)$ in the low x (0.0008-0.6) and Q^2 (0.2-75 (GeV)^2) range of the data [24].

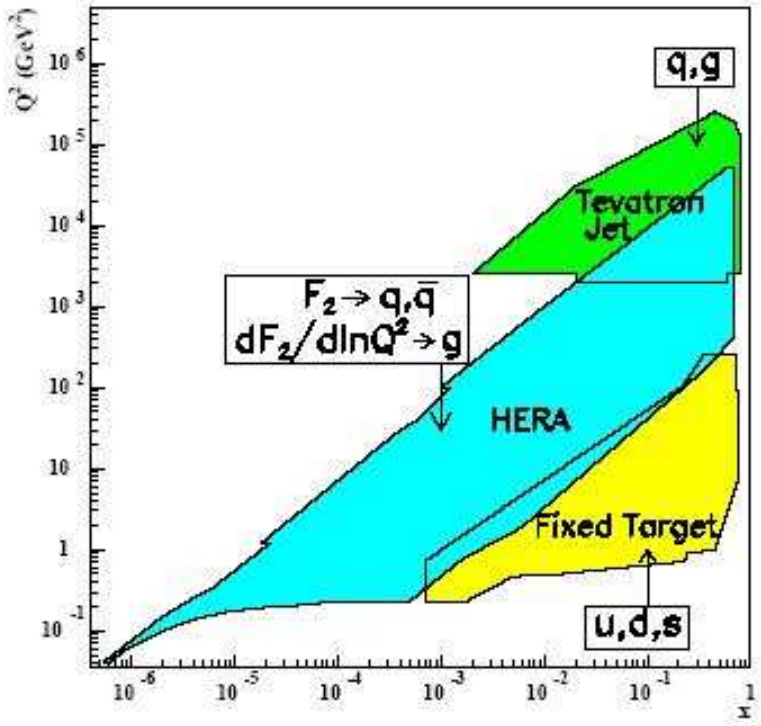

Figure 6.1: Ranges of kinematic variables x and Q^2 accessible to experiments realized up to now [2].

6.3 Experiments at HERA

The second way how to obtain collisions of protons with leptons at high energy is colliding. Such arrangement was possible to gain at the Hadron Electron Ring Accelerator (HERA) at Deutsches Electronen Synchrotron (DESY) at Hamburg. At HERA, colliding particles were electrons and positrons with energy of 27.6 GeV and protons with energy of 820 GeV (920 GeV after upgrade). The total CMS energy was $\sqrt{s}$ = 300.9 GeV (319.9 GeV after upgrade). Three typical analysis will be mentioned. ZEUS Collaboration [22] measured deep inelastic e^+p cross sections in the years 1996-1997. Proton structure function $F_2(x, Q^2)$ were prepared in the kinematic range 10^{-5} $\leq$ x $\leq$ 0.65 and 2.7 $\leq$ Q^2 $\leq$ 30 000 (GeV)^2. Integrated luminosity was of 30 pb^{-1}. H1 Collaboration [26] prepared $F_2(x, Q^2)$ as well as $F_L(x, Q^2)$ by measuring of deep inelastic $e^+ - p$ cross sections. The measurements covered the range 3 10^{-5} $\leq$ x $\leq$ 0.2 and 1.5 $\leq$ Q^2 $\leq$ 150 (GeV)^2. Integral luminosity was 20 pb^{-1}. Using low x H1 data it was possible to determine the gluon distribution $xg(x, Q^2)$.

An example of measuring structure functions at DESY is H1 Collaboration report [25]. This time the energy of proton beam was 920 GeV, corresponding CMS energy rose at $\sqrt{s}$=319 GeV and integrated luminosity rose at 65.2 pb^{-1}. Collaboration provided high Q^2 measurement of F_L and x$\tilde{F}_3$ in kinematic range 0.0013 $\leq$ x $\leq$ 0.65 and 100 $\leq$ Q^2 $\leq$ 30 000 (GeV)^2. These, data together with H1 low Q^2 precision data were used to perform new NLO QCD analysis in the framework of the Standard Model to extract parton distribution functions of the proton.

Table 6.1: Most important experiments measuring structure functions up to now.

	years	**x**	Q^2 **[(GeV)^2]**	**str. func.**
SLAC	1970-1985	6 10^{-2} - 0.90	0.6-30.0	F_2, R
BCDMS	1978-1985	6 10^{-2} - 0.80	7-260	F_2, R
NMC	1986-1989	2 10^{-3} - 0.60	0.5-75	F_2
		2 10^{-3} - 0.12	0.2-150	R
E665	1987-1992	8 10^{-4} - 0.60	0.2-75	F_2
H1	1996-1997	3 10^{-5} - 0.20	1.5-150	F_2, F_L
H1	1999-2000	1.3 10^{-2} - 0.65	100-30000	F_L, x$\tilde{F}_3$
ZEUS	1996-1997	6 10^{-5} - 0.65	2.7-30000	F_2

	events or int. lum.	**process**
SLAC		e(20GeV) + p
BCDMS	1.81 10^6	μ(280GeV) + p
NMC	2.36 10^6	μ(280GeV) + p
E665	159 853	μ(470GeV) + p
H1	20 pb^{-1}	e$^+$(27.6GeV) + p(820GeV), $\sqrt{s} = 300.9GeV$
H1	65 pb^{-1}	e$^+$(27.6GeV) + p(920GeV), $\sqrt{s} = 319.9GeV$
ZEUS	30 pb^{-1}	e$^+$(27.6GeV) + p(820GeV), $\sqrt{s} = 300.9GeV$

Chapter 7

Detector ATLAS

ATLAS (A Toroidal LHC ApparatuS) detector (drawn in Fig. 7.1) is one of four detectors at Large Hadron Collider (LHC) at CERN [10],[11]. The LHC will collide beams of protons with a center of mass energy of 14 TeV and a design luminosity of $10^{34} cm^{-2} s^{-1}$. The bunch crossing rate will be 40 MHz and at full luminosity there will be approximately 23 proton-proton collisions per bunch crossing. The rate of selected events will be reduced to $\sim$ 100 Hz for permanent storage by the trigger and data-acquisition system, which is based on three levels of online event selection [11].

The ATLAS level-1 trigger makes an initial selection based on reduced-granularity information from a subset of detectors. Events selected by level-1 trigger reduced to the maximum rate 75 kHz (upgraded 100 kHz) are read out from the front-end electronic system of the detectors into readout drivers (RODs) and then into readout buffers (ROBs). RODs and ROBs create a level-2 trigger, which decreases rate into max 1 kHz. The accepted data are transferred by data acquisition system to storage associated with the Event Filter, which makes the level-3 trigger. After event building, the full event is stored in a single memory accessible by an EF processor.

The ATLAS detector consists of four major components, the inner detector, calorimeters, the muon spectrometer, and magnet system. The overall detector has a typical cylinder-like shape with a total length of 42 m and a radius of 11 m.

The basic design criteria of the detector include very good electromagnetic calorimetry complemented by full-coverage hadronic calorimetry, high-precision muon momentum measurements, efficient tracking at high luminosity and full event reconstruction capability at lower luminosity, large ac-

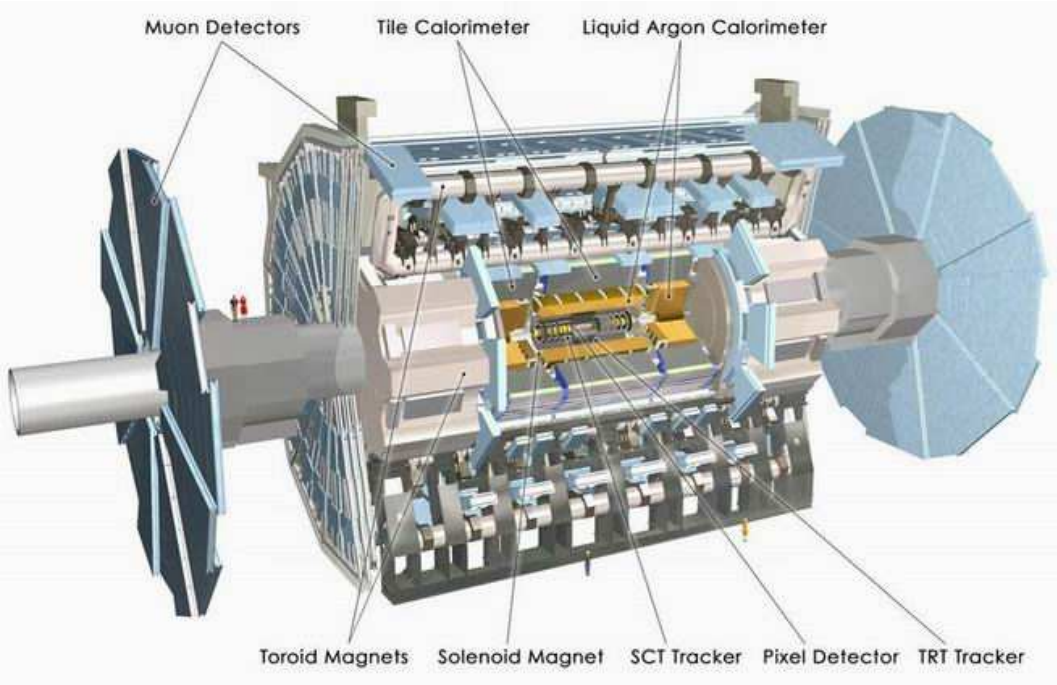

Figure 7.1: Overall layout of the ATLAS detector [44].

ceptance in pseudorapidity with almost full azimuthal angle coverage everywhere, and of course good triggering, see Fig.7.2.

The ATLAS coordinate system is a right-handed system with the x-axis pointing to the center of the LHC ring, the z-axis following the beam direction and y-axis going upwards. The azimuthal angle $\Phi = 0$ corresponds to the positive x-axis and Φ increases clock-wise looking into the positive z direction. The polar angle Θ is measured from the positive z-axis. Pseudorapidity, η, is defined by

$$\eta = -\log\Big(\tan\frac{\theta}{2}\Big). \tag{7.1}$$

Transverse momentum, p_T, is defined as the momentum component perpendicular to the LHC beam axis.

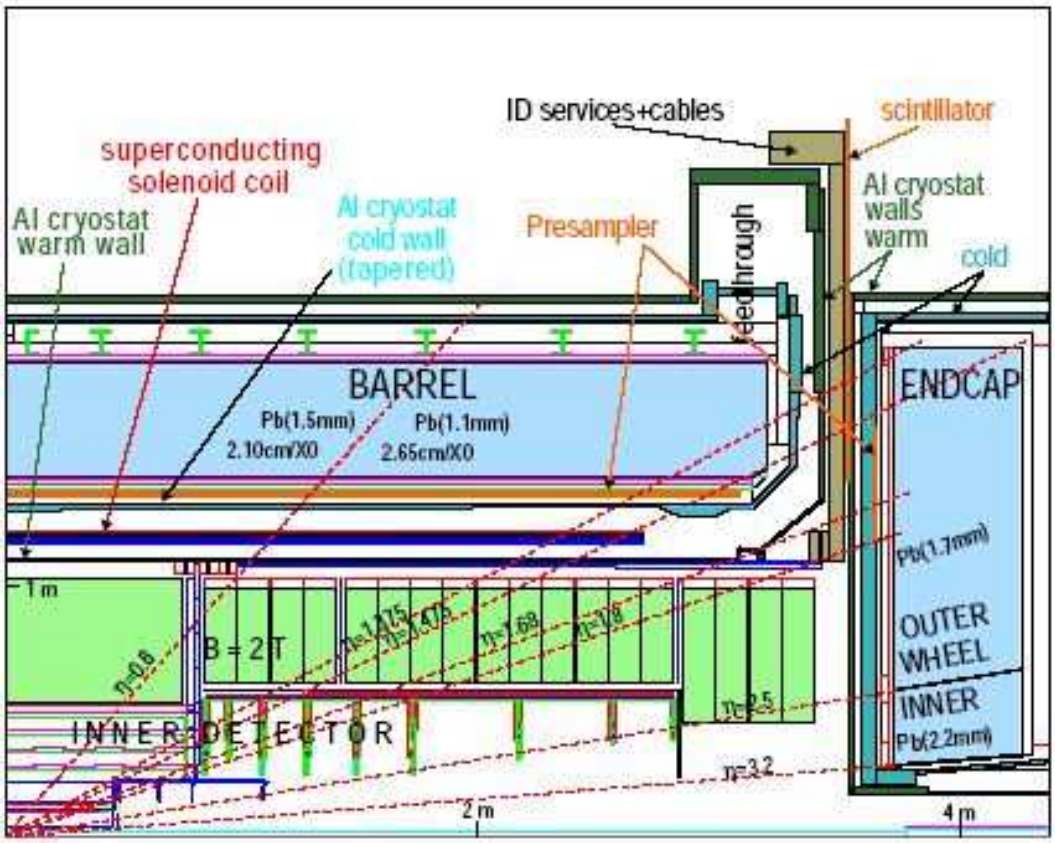

Figure 7.2: Assignment of the values of pseudorapidity to polar angle sketched in profile outline of the ATLAS detector [11](Figure 4-i).

7.1 Magnet system

The ATLAS superconducting magnet is an arrangement of a central solenoid (CS) and the toroid magnet system including two end-cap toroids (ECT). The central solenoid has a length of 5.3 m with a bore of 2.44 m and provide the inner detector with nominal magnetic field of 2 T. The CS coil is designed to be as thin as possible (19 cm) due to the position of the CS in front of the EM calorimeter. As a consequence, the CS and EM calorimeter share one common vacuum vessel and one cryostat.

The toroid magnet system consists of eight barrel toroids (BT) assembled radially and symmetrically around the beam axis, each housed in separate

cryostat and two end-cap magnets. Both of the two end-cap coil systems are build up of eight coils occupying one cryostat. The cryostat rests on a rail system facilitating the movement parking of the ECT magnets for access to the detector center.

The conductor used in all the coils is a composite that consists of a flat superconducting NbTi cable located in the center of an aluminium stabilizer with rectangular cross section. Sizes and compositions of the coils as well its operating currents are summarized in Table 7.1.

All the magnets are indirectly cooled by forced flow of helium at 4.5 K through tubes welded on the casing of the windings.

Table 7.1: Main parameters of the toroidal and solenoid magnets in the ATLAS magnet system.

Property	**Barrel Toroid**	**End-Cap Toroid (one)**	**Central Solenoid**
Inner diameter [m]	9.4	1.65	2.44
Outer diameter [m]	20.1	10.7	2.63
Axial length [m]	25.3	5	5.3
Number of coils	8	8	1
Operating current [kA]	20.5	20	7.6
Peak field [T]	3.9	4.1	2.6
Ratio Al:Cu:NbTi	28:1.3:1	19:1.3:1	15.6:0.9:1

7.2 Inner detector

The inner detector is contained within a cylinder of length 7 m and a radius of 1.15m. Mechanically, the ID consists of three units: a barrel part extending over $\pm$ 80 cm, and two identical end-caps covering the rest of the cylindrical cavity.

ID combines high-resolution silicon microstrip (SCT) and pixel detectors at the inner radii with continuous tracking elements (TRT) at the outer radii. The combination of two techniques gives very robust pattern recognition and high precision in both Φ and z coordinates.

In the barrel region, the high-precision detector layers are arranged on concentric cylinders around the beam axis, while the end-cap detectors are mounted on disks perpendicular to the beam axis. The highest granularity is achieved around the vertex region using semiconductor trackers and pixel detectors. The total number of the layers must be limited because of their cost. Typically, three pixel layers and two times four strip layers are crossed by each track. A large number of tracking points (typically 36 per track) is provided by the straw tube tracker.

The first layer of pixel detectors is at radii of 4 cm from the beam pipe. The lifetime of such a detector will be limited by radiation damage. It is therefore considered very important that this innermost pixel layer (or B layer) can be replaced.

The pixel detector is designed to provide a very high-granularity, high-precision set of measurements as close to the interaction point as possible. The system provides three precision measurements over full acceptance, and mostly determines the impact parameter resolution and the ability of the inner detector to find short-lived particles such as B hadrons and τ leptons. The system consists of three barrels at radii of 50.5 mm, 88.5 mm, and 122.5 mm, and three discs on each side, between radii of 11 and 20 cm, which complete the angular coverage. The system contains a total of 140 million detector elements, each 50 μm in the $R\Phi$ direction and 300 μm in z.

The SCT system is designed to provide eight precision measurements per track in the intermediate radial range by the use of high granularity and so contributes to the measurements of momentum, impact parameter, vertex position and pattern recognition. Each of eight layers of silicon microstrip detectors measure one point in the RΦ or using small angle stereo in z coordinate. From these four pairs of points are reconstructed four space points per track. Each silicon detector is 6.36 x 6.40 cm with 768 readout strips of 80 μm pitch.

The TRT system is based on the use of combination of straw trackers, which can operate at very high rates expected at the LHC, and transition radiation detectors, which detect transition-radiation photons created in a radiator between the straws. Each straw is 4 mm in diameter and equipped with a 30 μm diameter gold-plated W-Re wire. The TRT is operated with a non-flammable gas mixture of 70% Xe, 20% CO_2 and 10% CF_4, with a total volume of 3 m^3. The barrel part contains 52 544 axial straws of 144 cm length. The end-caps contain a total of 319 488 radial straws.

Detailed parameters of individual parts of inner detector are recapitulated

in Table 7.2.

Table 7.2: Parameters of the inner detector.

System	**Position**	**Resolution** $\sigma(\mu\mathbf{m})$	**Channels** (10^6)	η **coverage**
Pixels	1 removable barrel layer	RΦ=12, z=66	16	± 2.5
	2 barrel layers	RΦ=12, z=66	81	± 1.7
	5 end-caps discs on each side	RΦ=12, z=77	43	1.7-2.5
Silicon strips	4 barrel layers	RΦ=16, z=580	3.2	± 1.4
	9 end-caps wheels on each side	RΦ=16, z=580	3.0	1.4-2.5
TRT	Axial barrel straws	170 per straw	0.1	± 0.7
	Radial end-cap straws	170 per straw	0.32	0.7-2.5

7.3 Calorimeter

For the construction of the ATLAS calorimeters is used two fundamental types of sampling calorimeters: the liquid argon (LAr) calorimeter for both electromagnetic and hadronic calorimetry and the tile calorimeter for hadronic calorimetry [11]. The full pseudorapidity coverage (±4.9) is obtained by typical layout of the calorimeters in the barrel and end-cap regions and in forward region very close to the beam-pipe. The cutaway of one side of detector is shown in Fig. 7.3. The disadvantage of the LAr calorimeters is the cooling. The EM LAr calorimeter in the barrel region is contained in a barrel cryostat together with the central solenoid cavity. Two end-cap cryostats house the end-cap EM and hadronic LAr calorimeters, as well as the integrated forward calorimeter. Due to cryostat walls and the barrel solenoid presamplers consisted of one active layer (1.1 cm barrel, 0.5 cm and-cap) of LAr are located in front of the EM calorimeters and help to correct for the energy loss. The region $1.37 < |\eta| < 1.52$ is not used for precision physics measurements involving photons because of the large amount of non-active material situated in front of the EM calorimeter.

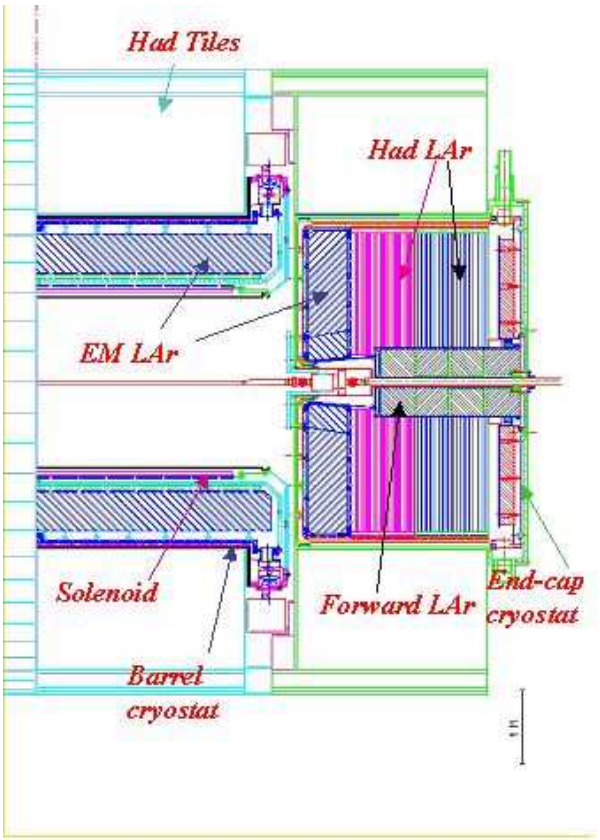

Figure 7.3: Two-dimensional cutaway view of the ATLAS calorimeters [45].

The barrel EM calorimeter is divided into two identical half-barrel parts ($|\eta| < 1.475$), separated by a small gap (6 mm) at $z = 0$. Each EM end-cap calorimeter is mechanically divided into two coaxial wheels ($1.375 < |\eta| < 3.2$). The EM sampling LAr calorimeter has lead accordion-shaped electrodes and lead absorber plates over its full η coverage. The accordion geometry provides complete Φ symmetry without azimuthal cracks. The EM calorimeter is segmented into three longitudinal sections. The first strip section equipped with narrow strips acts as a "preshower" detector and provides enhancing particle identification and a precise position measurement in η. The middle section is transversally segmented into square towers of size $\Delta\eta \times \Delta\Phi = 0.025 \times 0.025$. The back section has a granularity of 0.05 in η. The total thickness of the EM calorimeter is > 24 radiation lengths (X_0) in the barrel and > 26

X_0 in the end-caps. The total number of channels is ∼190 000.

For hadronic calorimetry, different techniques for the widely varying requirements and radiation environment over the large η range are used. The iron scintillating-tile technique is used for the barrel ($|\eta| < 1.0$), two extended barrel calorimeters ($0.8 < |\eta| < 1.7$), and for intermediate tile calorimeter (ITC) in the gap between them. This gap provides space for cables and services from the innermost detectors. The LAr sampling type of calorimeters is chosen for end-cap ($1.5 < |\eta| < 3.2$) calorimeters (HEC) and for high-density forward calorimeter (FCAL) covering region $3.1 < |\eta| < 4.9$.

The total thickness of the hadronic calorimeters is 11 interaction lengths at $\eta = 0$ and is designed to provide good containment for hadronic showers and reduce punch-through into the muon system to a minimum.

The structure of tile calorimeter is periodic along the z-axis and is cylindrical formed with a inner radius of 2.28 m and an outer radius of 4.23 m. The 14 mm thick iron plates of the absorber alternate with scintillating tiles as the active material. Two sides of the scintillating tiles are read out by wavelength shifting fibres into two separate photomultipliers. The total number of channels is about 10 000.

For hadronic end-cap calorimeters, as well as for FCAL, LAr method of calorimetry with better granularity than at TILECAL is used because of their position and importance of good E_T^{miss} measurements despite their higher complexity. Each HEC consists of two independent copper wheels of thickness 50 mm (closer to the interaction point) and 25 mm (the upstream wheel). In both wheels, the 8.5 mm gap between consecutive copper plates is equipped with three parallel electrodes, splitting the gap into four drift spaces of about 1.8 mm. This electrode structure forms an electrostatic transformer (EST) with an EST ratio of two.

The FCAL is particularly challenging detector owing to the high level of radiation it has to cope with ($3.1 < |\eta| < 4.9$). Such amount radiation calls for a high-density design. The FCAL consists of three sections: the first one is made of copper, while the other two are made out of tungsten. In each section the calorimeters consist of a metal matrix with regularly spaced longitudinal channels filed with concentric rods and tubes. The rods are positive high voltage while tubes and matrix are grounded. The LAr in the gap between is the sensitive medium. The geometry allows for an excellent control of the gaps witch are as small as 250 μm in the first section. For tungsten sections has been chosen a technique based on the assembly of small sintered tungsten alloy pieces. The overall density (including argon) of

a section built in this way, with 975 μm gaps, is 14.5 g/cm^3. The number of FCAL channels is 3 584 for the total of both sides.

7.4 Muon spectrometer

Only muons are heavy and long-lived enough, non-strongly interacting particles that pass through the calorimeters and reach the outermost parts of the detector. The muon spectroscopy is based on the deflection of muon tracks in the strong magnetic field and high precision tracking chambers. On the other hand, the secondary particles, produced from interactions in the calorimeters, shielding material, beam pipe, and LHC machine elements, create a difficult background and demand optimized reconstruction algorithms and trigger.

In the barrel region ($|\eta| < 1.0$) muons are measured in three layers of chambers concentric with the beam axis at radii of about 5, 7.5, and 10 m. The precision of the track coordinates is provided by Monitored Drift Tubes (MDTs). Trigger system uses fast Resistive Plate Chambers (RPCs). In the region of larger pseudorapidity are installed Cathode Strips Chambers (CSCs) with higher granularity. In the end-cap region ($1.0 < |\eta| < 2.7$), the same precision chambers are used: CSCs in the innermost plane and MDTs. For triggering, Thin Gap Chambers (TGCs) are used. Main characteristics of parts of muon spectrometer are in Table 7.3.

Table 7.3: Basic parameters of the four types of muon chambers.

	Precision chambers		**Trigger chambers**	
	CSC	**MDT**	**RPC**	**TGC**
Number of chambers	32	1 194	596	192
Number of channels	67 000	370 000	355 000	440 000
Area covered [m^2]	27	5 500	3 650	2 900

The basic detection elements of the MDT chambers are aluminium tubes of 30 mm diameter and 400 microns wall thickness, with a 50 microns diameter central W-Re wire. The tube lengths vary from 70 cm to 630 cm. The tubes are operated with a non-flammable mixture of 93% Ar and 7% CO_2 at 3 bar absolute pressure and have a total volume of 800 m^3. Mechanical

deformations are monitored by an in-plane optical system, hence the name "monitored drift-tube chambers".

The CSCs are multiwire proportional chambers with cathode strip readout. The cathode strips for the precision measurement are orthogonal to the anode wires. The anode wire pitch is 2.54 mm and the cathode readout pitch is 5.08 mm. The precision coordinate is obtained by measuring the charge induced on the segmented cathode by the avalanche formed on the anode wire. Good spatial resolution is achieved by segmentation of the readout cathode and by charge interpolation between neighboring strips. The baseline CSC gas is a non-flammable mixture of 30% Ar, 50% CO_2 and 20% CF_4, with a total volume of 1.1 m^3.

The RPC is a gaseous detector. The basic RPC unit as a narrow gas gap formed by two parallel resistive 2 mm thick bakelite plates, separated by polycarbonate spacers of 2 mm thickness which define the size of the gas gap. The gas mixture is based on tetrachloroethane ($C_2H_2F_4$) with some small admixture of SF_6, a non-flammable and environmentally safe gas that allows for relatively low operating voltage. The signal is read out via capacitive coupling by metal strips on both sides of the detector. The readout strips are arranged with a pitch varying from 30.0 to 39.5 mm. A trigger chamber is made from two rectangular detector layers, each one read out by two orthogonal series of pick-up strips: the "η strips" are parallel to the MDT wires and provide the bending view of the trigger detector, the "Φ strips", orthogonal to the MDT wires, provide the second-coordinate measurement witch is also required for the offline pattern recognition.

The TGCs are similar in design to multiwire proportional chambers operated with a highly quenching gas mixture of 55% CO_2 and 45% n-pentane (n-C_5H_{12}), with the difference that the anode wire pitch is larger than the cathode-anode distance. This type of cell geometry permits operation in saturated mode, with a number of advantages. The total gas volume is 16 m^3. The gas mixture is highly flammable and requires adequate safety precautions. The main dimensional characteristics of the chambers are a cathode-cathode distance (gas gap) of 2.8 mm, a wire pitch of 1.8 mm, and a wire diameter of 50 μm.

Chapter 8

The ATLAS physics program

The physics program planed to be performed at ATLAS is shortly reviewed in this chapter. This topic is comprehensively reviewed in [12], [33].

Technical parameters of the ATLAS detector were described in Chapter 7 and the need of precise measurement was mentioned as well. The excellent performance of the detector ATLAS together with the high energy and luminosity of the LHC offer a great potential for the Higgs boson searches as well as for observability of a variety of other physics processes. It includes studies of hadronic physics, precision measurements in the Standard Model area and CP violation phenomena, continuing through the searches for supersymetry, to a discussion of new physics beyond Standard Model.

The dominant background for a new physics searches is created by QCD processes which will provide a powerful device for testing and extending of the Standard Model. This will be followed by precise measurements of the properties of the W and Z bosons, their masses and couplings. Next are the investigations of CP violation in B decays, D_s^0 oscillations, top quark and heavy leptons production. The one of the most challenging physics goals are the various Higgs boson searches. The physics program contains also theories beyond Standard Model like SUSY, technicolor, Majorana neutrinos and the fourth generation of quarks.

8.1 QCD processes

The study of QCD processes can be divided into two main areas according to their goals. At first, a large number of precise measurement will be per-

formed in the early stages of the experiment at low luminosity. They will test the predictions of QCD and allow to establish additional constraints, e.g. the strong coupling constant α_s at various scales. Test of QCD can be accomplished by comparing measurements to theoretical calculations, prepared at most by Monte Carlo programs.

Second part of investigation of QCD processes will be performed in a new energy regime with high statistics. The main goal is precise understanding of QCD processes which create the background of other important Standard Model processes. Deviations from QCD expectations might indicate the occurrence of new physics. The special attention will be turned to jet and photon physics, open charm and beauty production and gauge bosons production. Precise constraints on the parton distribution functions will be derived from measurements of Drell-Yan production, of production of W and Z boson, of direct photons and high p_T jets, heavy flavors and gauge boson pairs.

The analysis of parton kinematics will be performed at the ATLAS as well. Data from ATLAS can be included to the global fitting programs, where it will serve to confirm or constrain the parton distribution functions in the kinematic range of LHC. Generally, Drell-Yan production will provide information on the quark and anti-quark distribution while direct photon, jet and top production will provide, in addition, information on the gluon distribution.

As mentioned above, QCD processes will create a gigantic amount of data, especially in the region near the beam-pipe. The knowledge of the structure of these minimum-bias events is for a great importance for all physics at ATLAS as well as a diagnostic tool on the performance of the detector. In order to have a efficient detection of minimum-bias events, and to allow for a minimization of uncertainties in the extrapolation due to the modeling of minimum-bias events, a very small acceptance loss is desirable. It can be satisfied by installation of additional detectors in the forward region close to the beam-pipe outside of the ATLAS detector.

In the last few years an understanding of diffractive phenomena attracted a new attention due to the appearance of diffractive processes in a hard scale, i.e. hard diffractive scattering. These are inclusive processes $p + p \rightarrow p + X$, where X contains a hard scattering. Hard diffractive scattering is expected to be part of the inclusive hard scattering cross section. The information about dynamics of this process is suggested to be provided by measurements of jets, W/Z, direct photon and heavy flavor production. The name diffraction

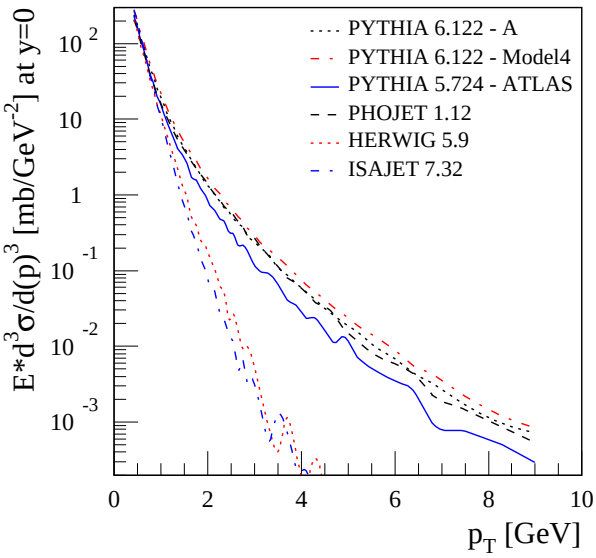

Figure 8.1: Transverse momentum spectrum of charged particles in minimum bias events at LHC energies, for six model predictions. For the HERWIG and ISAJET calculations, no hard scattering processes have been included. [12](Figure 15-13)

is derived from the behavior of cross section for these events as a function of the momentum transfer, reminiscent of the properties of the diffraction of light on a circular aperture. The advantage of LHC is the production of diffractive final states with larger masses, allowing further understanding of the transition between perturbative and non-perturbative QCD.

The measurement of jets, i.e. particles with a large total transverse momentum, will be the most important for studying of hard scattering processes. The selection of inclusive jet production will be based on an inclusive jet trigger with a threshold of $180GeV$ at low luminosity ($290GeV$ at high luminosity), where jets have to be within $|\eta| \leq 3.2$. The measurement of jets demand to take into account the evolution of the partonic system from the hard scattering to the observed set of hadrons. This task involves inclusion of parton showering, fragmentation and multiple parton scattering.

The detection of photons at the LHC will be a challenging task due to the large background from jet production. However, the fine calorimeter-granularity offers the possibility for a large suppression of jet background

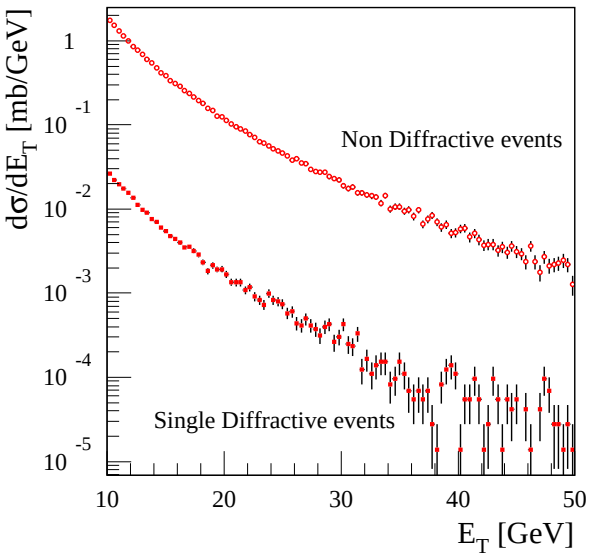

Figure 8.2: Cross section for di-jet production ($|\eta^{jet}| < 3.2$) as a function of the jet transverse energy for non-diffractive and single diffractive events, obtained from the PHOJET Monte Carlo model. [12](Figure 15-16)

and provides a good energy determination. Direct photon measurements can provide important constraints on parton distributions, photon pair production will help for Higgs boson searches.

8.2 Physics of electroweak gauge bosons

The LHC will abundantly produce gauge bosons as well gauge boson pairs. Measurements performed at ATLAS will significantly improve the precision achieved at present machines owing to the large statistics and the high center of mass energy.

One of the main goals is to increase the precision in W boson mass measurement from about $30MeV$ at LEP2 to about $20MeV$. This error should decrease to about $15MeV$ by combining ATLAS and CMS together. The W mass is related to the QED fine structure constant α,the Fermi constant G_F, Weinberg angle $\sin\theta_W$ and to the radiative corrections, which depend on

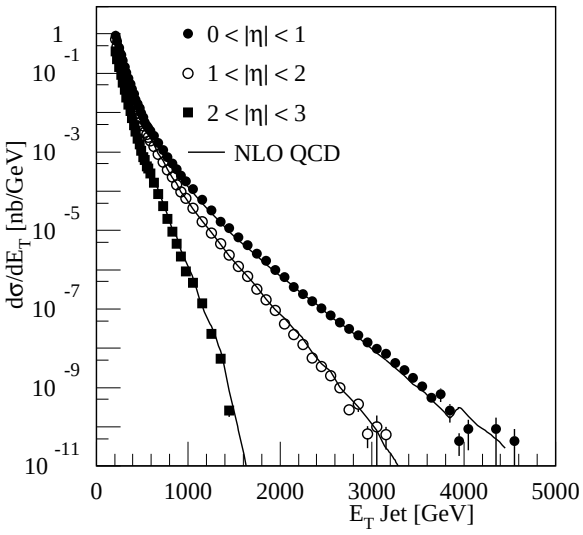

Figure 8.3: Inclusive jet cross section (at hadron level) for different ranges of the jet pseudorapidity obtained from a PYTHIA calculation (points) and from a NLO Monte Carlo calculation (solid line). [12](Figure 15-22)

other Standard Model parameters like top and Higgs mass. Another problem is detection of neutrinos, because the measurement of the W mass is performed at hadron colliders in the leptonic channels. This method leads to the use of transverse mass m_T^W. The distribution of m_T^W, and in particular the trailing edge of the spectrum, is sensitive to the W mass. The W mass is therefore obtained by fitting the experimental distribution of transversal mass.

The powerful test of the Standard Model, which is based on the gauge invariance, will be measurement of the triple gauge boson coupling (TGC) and quadruple gauge boson couplings (QGC). The precise measurements of the couplings will not only be a stringent test of the SM and the electro-weak symmetry breaking, but also probe for new physics. Deviations in the values of coupling from supersymmetric or technicolor corrections are comparable to the Standard Model radiative corrections. Experiment that can reach this sensitivity could provide powerful constraints on these models.

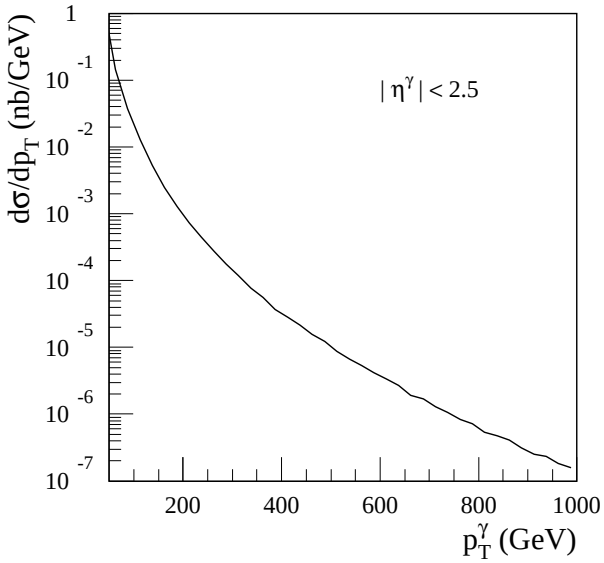

Figure 8.4: Inclusive direct photon cross section at leading order (from PYTHIA, including the ATLFAST detector simulation) as a function of p_T for the CTEQ3L pdf. [12](Figure 15-33)

8.3 B-physics

Although LHCb experiment is dedicated for B-physics, the ATLAS experiment will be competitive in several channels. The main goal is then to obtain a maximized combined precision from the whole LHC. The potential of ATLAS is in production and triggering of B-hadrons and CP violation measurement in a number of channels.

CP violation is represented in the Standard Model by the phase of the CKM quark-mixing matrix. The unitarity of the CKM matrix leads to the triangle relations with angles α, β, γ. These angles can be measured,for example, in neutral B decays with the same final state. The CP violation amplitude can be derived from asymmetry between B^0 and $\bar{B^0}$ decay rates. One of the preferred decay is e.g. $B_d^0 \to J/\psi K_s^0$.

A phenomena of B_s^0 oscillation is predicted by the Standard Model but it has not yet been observed directly. The non-conservation of flavor in charged weak current interactions allow transitions between B_s^0 and $\bar{B_s^0}$ states with

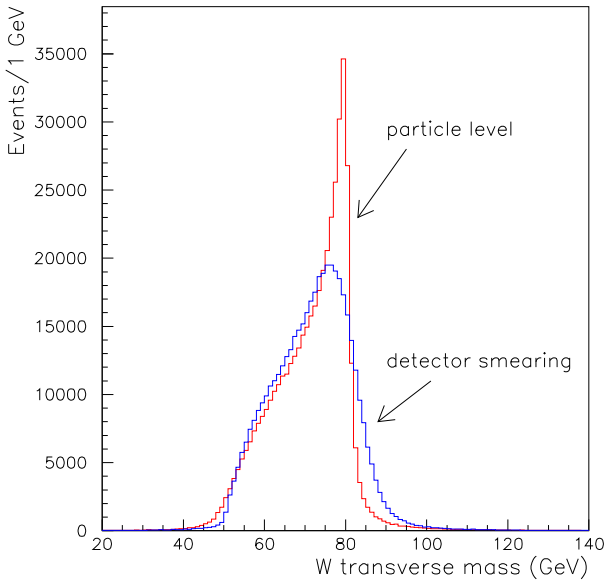

Figure 8.5: Distribution of the W transverse mass as obtained at particle level and by including the expected ATLAS detector resolution. [12](Figure 16-1)

a frequency proportional to Δm_s. The oscillation period can be determined by fitting of the special asymmetry between B_s^0 and $\bar{B}_s^0$.

8.4 Heavy quarks and leptons

The LHC, with its beam energy and luminosity, will produce $t\bar{t}$ pairs with the cross section about 100 times greater than that at Tevatron. Studies of these millions of $t\bar{t}$ events and single top quark events will allow detailed measurement of the properties of the top quark. The high mass of the top quark will permit studies of the electroweak symmetry breaking through the large variety of top decays. The accurate measurement of the top quark mass helps constrain the mass of the Standard Model Higgs boson. In addition, the existence of fourth generation quarks and new heavy leptons will be probed for masses up to of order $700GeV$.

According to the Standard Model, the top quark decays almost exclusively to Wb. The final states of $t\bar{t}$ events then depends on the decay channel of the W boson. The hadronic decay mode of the W boson is more probable

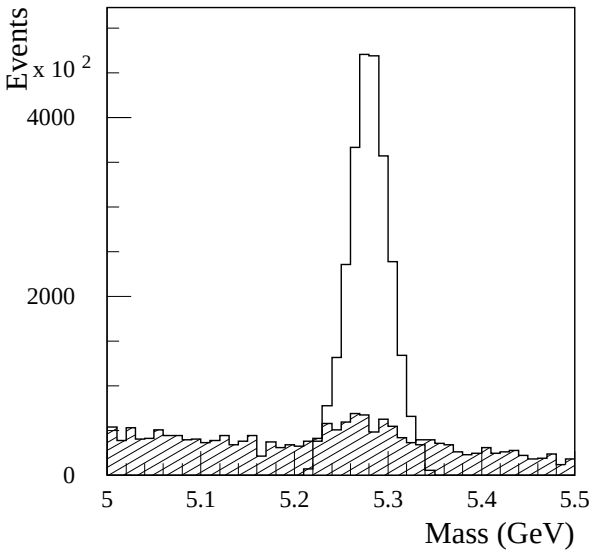

Figure 8.6: Invariant mass distribution of the decay $B_d^0 \rightarrow J/\psi(\mu\mu)K^{*0}$ (open histogram) with superimposed the estimated background contribution (shaded histogram). [12](Figure 17-10)

but these events are difficult to distinguish from the large QCD multi-jet background. For that reason the analysis of $t\bar{t}$ events will be concentrated to the leptonic channels $W \rightarrow l\nu$.

The mass of the top quark is a fundamental parameter of the SM and should be measured as accurately as possible. The current value of top quark mass is $m_t = 174.3 \pm 3.2 \pm 4.0 GeV$ from CDF and D0 experiments. The new precision would be $\delta m_t \leq \pm 2 GeV$. The supersymmetric model would offer even better precision from top-bottom-tau Yukawa coupling measurement.

8.5 Higgs bosons

The ATLAS detector will have a large potential (see Fig. 8.8) in the investigation of one of the key physics questions at LHC, the origin of electroweak symmetry breaking. The observation of one or several Higgs bosons will provide a better understanding of the mechanism of electroweak symmetry

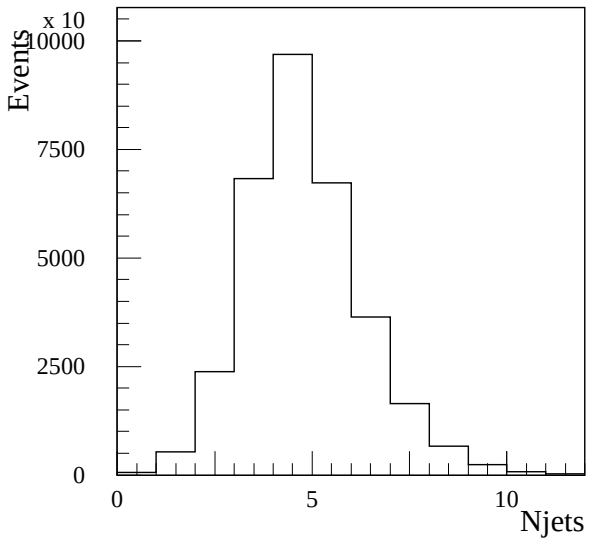

Figure 8.7: Distribution of jet multiplicity (threshold at $p_T > 20GeV$) for single lepton plus jet events with a lepton $p_T > 20GeV$, normalized to an integrated luminosity of $10fb^{-1}$. [12](Figure 18-3)

breaking. On the other hand, the non-observation of any Higgs boson will cause many difficulties and changes in Standard Model at all.

The Standard Model predicts an existence of one neutral scalar Higgs particle H. The mass of this H is not theoretically determined besides an upper limit of about $1TeV$ from the unitarity arguments. Experimental constraint to the mass of H is $m_H > 90GeV$ from searches at LEP2.

The various decay channels have been established through many studies for Standard Model Higgs boson searches. The dominance of individual channel depends on the H mass region. Generally, the most important channels are $H \rightarrow WW^*$, where jets or leptons can be in the final state, the four lepton channel, $H \rightarrow ZZ^* \rightarrow 4l$, the direct two-photon channel, $H \rightarrow \gamma\gamma$, as well as the associated production channels, where H is produced in association with a vector boson or $t\bar{t}$ pair.

Supersymmetric theories rapidly extend the Higgs sector. Minimal Supersymmetric Standard Model (MSSM model) deals with five physical Higgs particles: two CP-even h, H, one CP-odd A, and two charged $H^{\pm}$. The

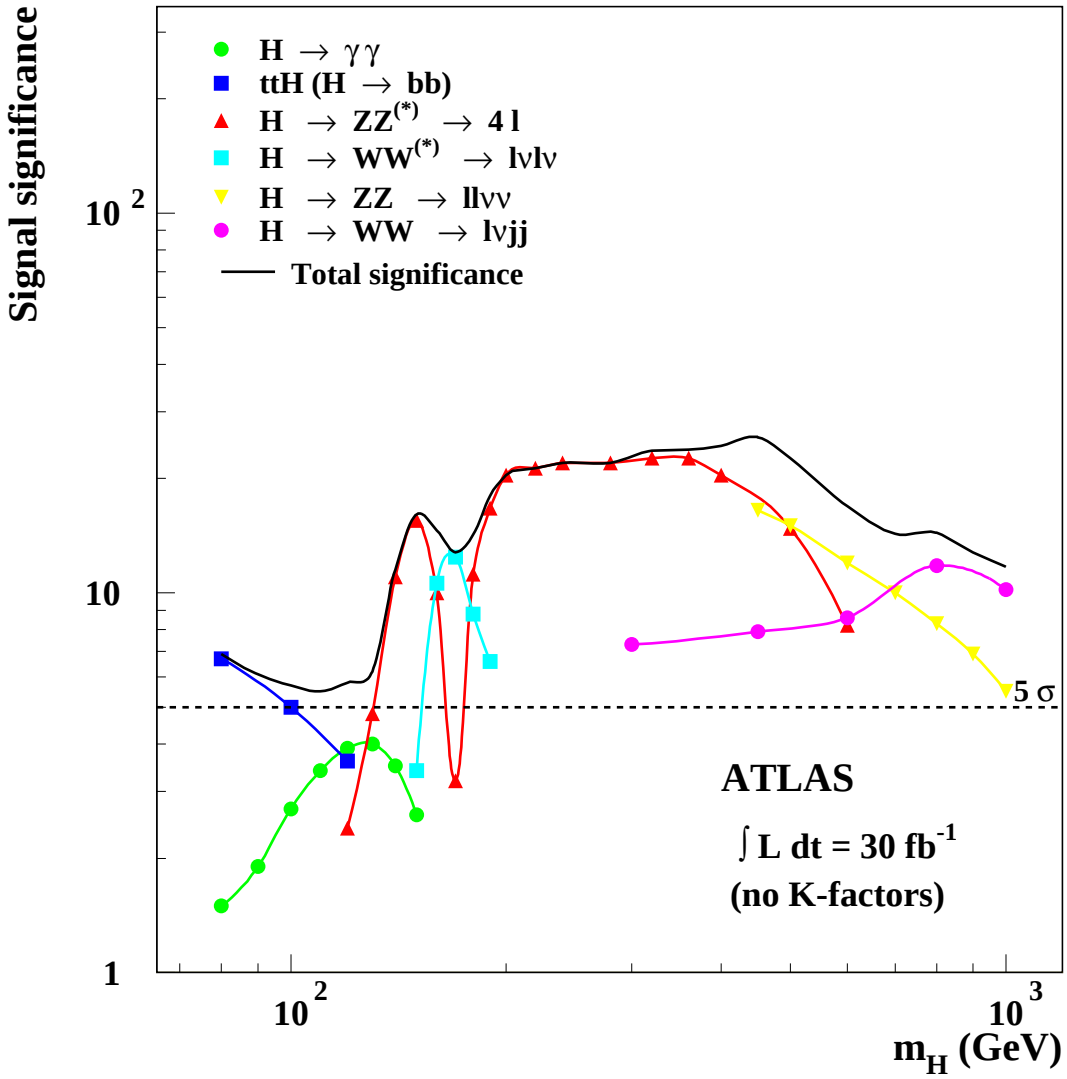

Figure 8.8: ATLAS sensitivity for the discovery of a Standard Model Higgs boson. The statistical significances are plotted for individual channels, as well as for the combination of all channels, assuming integrated luminosities of $30 fb^{-1}$ (top) and $100 fb^{-1}$ (bottom). Depending on the numbers of signal and background events, the statistical significance has been calculated as $S\sqrt{B}$ or using Poisson statistics. [12](Figure 19-i)

experiment would be able to distinguish between the SM and the MSSM models for almost all channels.

8.6 Supersymmetry

The most promising theory from the large amount of 'beyond Standard Model' theories is Supersymmetry (SUSY).

SUSY is the maximal possible extension of the Lorentz group. It has fermionic generators $Q, \bar{Q}$ which satisfy

$$\{Q, \bar{Q}\} = -2\gamma_\mu P^\mu$$

$$[Q, P^\mu] = \{Q, Q\} = \{\bar{Q}, \bar{Q}\} = 0 \tag{8.1}$$

where P^μ is the momentum operator and γ_μ are the Dirac matrices. SUSY therefore relates particles with the same mass and other quantum numbers differing by $\pm 1/2$ unit of spin (squarks, gluinos, Higsinos, ...). The symmetry must of course be broken, since several superparticles have not been observed, e.g. selectron.

The Standard Model Laqrangian conserves baryon and lepton number. In SUSY it is possible to violate both. The consequence of this property of SUSY is for example weak-scale proton decay. A new invariance was imposed, R-rapidity conservation:

$$R = (-1)^{3(B-L)+2S}, \tag{8.2}$$

where B,L, and S are baryon number, lepton number, and spin. Hence R equals +1 for all Standard Model particles and R equals -1 for all SUSY particles.

The great advantage of SUSY is that implies an equal number of bosons and fermions and so cancels the quadratic divergences in loop corrections of the Higgs generation of mass. It provides a solution of the hierarchy problem, that incorporates a loop corrections at Planck (gravitational) mass scale. This is know as supergravity model (SUGRA).

Chapter 9

Monte Carlo event generators

Monte Carlo event generators for high-energy processes were evolved in order to model interactions of different particles and to predict the values of kinematic quantities observed in real experiments. The programs provide simulations of lepton-lepton, lepton-hadron and hadron-hadron scattering. The algorithm of event generation of Pythia and Herwig programs are discussed in this chapter in detail. Events generated by these programs are used further in this study.

Herwig and Pythia are general-purpose event generators based on different models of fragmentation mechanism comprehensively described in their manuals. It is Lund's string model of hadronization in Pythia [19] and Cluster model of hadronization in Herwig[18].

The typical high-energy event is described by an event generator simply as follows: a pair of incoming beam particles are characterized by two sets of parton distributions, which define the partonic substructure in terms of flavor composition and energy sharing. Each of an incident beam hadrons can radiate time-like partons and so starts off building up an initial-state shower.

One parton from each of the two initial showers collide and participate in hard subprocess. This can be described by exactly calculated matrix elements in lowest order of perturbation theory. The nature of this hard subprocess determines the main characteristics of the event. The outgoing partons may create a similar shower (final-state shower) like ingoing partons.

Strictly speaking, there are two approaches how to determine the event structure. One is the matrix element method, in which the exact kinematics is calculated order by order. This approach is used only for calculation the

main hard processes. The problem of this method is the increasing difficulty with increasing order. Mostly, the one loop is calculated in full.

The second approach is the parton shower one. The full matrix elements are not used, but only approximations derived by simplifying the kinematics, and the interference and helicity structure. Although parton showers have a limited predictive power they may, in practice, be matched to the first order matrix elements to describe the hard gluon emissions well.

During the event generation, the parton shower modeling is the first choice because of its simplicity and flexibility. The matrix elements are calculated mainly for α_s determination, angular distribution of jets, triple gluon vertex studies, and other specialized studies.

The most relevant parameters of the hard subprocess in the theoretical analysis of the showering are the hard scale Q and the energy fraction x of the incoming parton after the emission of initial-state radiation. For lepton-hadron processes x corresponds to the Bjorken variable, while for hadron-hadron processes x is related to Q^2/s. The initial-state radiations are space-like,i.e. partons have $m^2 = E^2 - \vec{p}^2 < 0$, the final-state radiations are time-like, i.e. $m^2 = E^2 - \vec{p}^2 \geq 0$. The initial as well as final state emission processes factorize and can be described as a coherent branching processes suitable for Monte Carlo simulations.

Initial-state radiation is handled within a backwards evolution scheme. In this approach, the choice of the hard scattering is based on the use of evolved parton distributions, which means that the inclusive effects of initial-state radiation are already included. The construction of exclusive showers remains. This is done starting from the two incoming partons at the hard interaction, tracing the shower backwards in time, back to the two shower initiators.

For large x, the coherent branching algorithm sums correctly not only the leading but also the next-to-leading contributions. In the case of small values of x, the initial-state branching process has additional properties, which are not yet fully included in event generators.

The coherent branching algorithm for final-state showering is described in terms of the parton energy fraction and the emission angle ξ. The values of the energy fraction are distributed according to the DGLAP splitting functions and the distribution of ξ value is determined by the Sudakov form factors. Angular ordering implies that each ξ value must be smaller than the ξ value for the previous branching of the parent parton. Showering from any parton stops when a value of ξ below Q_i^2/E_i^2 is selected for the next

branching.

In addition to the hard process many semihard or soft QCD processes, such as diffractive and elastic scattering and minimum-bias events, occur between the other partons of two incoming showers. These processes take place at low momentum transfer scale, for which the strong coupling α_s is large. Perturbation theory is not applicable and some phenomenological model has to be used.

The combination of the not observable outgoing gluons and quarks into observable mesons and baryons is non-perturbative process called hadronization. This is implemented differently in each of the event generators.

The HERWIG's cluster model for hadron formation, remnant hadronization and the underlying event is local in color and independent of the hard process and the energy. After the perturbative parton showering, all outgoing gluons are split non-perturbatively, into light quark-antiquark or diquark-antidiquark pairs. In the limit of a large number of colors, each final-state color line can be followed from a quark/antidoquark to an antiquark/diquark with which it can form a color-singlet cluster. These clusters are then turned into hadrons. If a cluster is too light to decay into two hadrons, its mass is shifted to the appropriate value by an exchange of fourmomentum with a neighboring cluster in the jet. The process of hadronization in Herwig program can be improved by adding the Jimmy program as done in this analysis.

The Pythia's string model of fragmentation is based on physical picture of QCD quark dynamics. As the quark and antiquark partons move apart from their common production vertex, the color flux tube is stretched between the q and the $\bar{q}$, i.e. energy is stored in the color dipole field between a charge and an anticharge. If the tube is assumed to be uniform along its length, this automatically leads to a confinement picture with a linearly rising potential. As the q and $\bar{q}$ move apart, the potential energy in the string increases, and the string may break by the production of a new $q'\bar{q}'$ pair. The system is now split into two color singlets $q\bar{q}'$ and $q'\bar{q}$. The string brake-up process is assumed to proceed until only on-mass-shell hadrons remain.

Chapter 10

Statistical tests of the goodness of fit

There are many tests of statistical hypotheses about values of unknown parameters of distribution of experimental data sample. This chapter compiles such statistical methods that are able to test wider hypotheses describing not only parameters of distributions of samplings but examining also the whole shape of this distribution. Two different tests are the most used ones: χ^2 test and Kolmogorov-Smirnov test. Both of these tests make possible to determine on validity or invalidity of the null-hypothesis at the predefined confidence level α. The null-hypothesis is defined as an assertion that the chosen distributions are identical. An alternative hypothesis is that these distributions are not identical. Two similar tasks can be distinguished according to the null-hypothesis. It can be either comparison between real distribution of data sample and theoretically expected distribution or comparison between distributions of two different data samples.

10.1 χ^2 test

The basic idea of this method is to dispose the aggregate of data into many disjoint subsets (classes). This way is often called binning of data. The value of the χ^2 test depends on how the data is binned [39]. The second main disadvantage is that the χ^2 approximation requires a sufficient sample size to be valid.

χ^2 test of the goodness of fit is a simple test based on the differences

between observed and expected frequencies of these classes or on the differences between observed frequencies of two different data samples. Let's consider aggregate of all measured data A with the number of events n and its classes $A_i,\ i = 1, \ldots, k$. Frequencies of events in A_i classes are denoted as n_i. The frequencies of events for the second data aggregate B in B_i classes are denoted as m_i. Frequencies for theoretical distribution can be considered as g_i which are predicted according to theoretical distribution with variance σ^2. It is obvious that

$$\sum_{i=1}^{k} g_i = n. \tag{10.1}$$

The sum of squares

$$\chi^2 = \sum_{i=1}^{k} \frac{(n_i - g_i)^2}{\sigma_i^2} \tag{10.2}$$

then follows the χ^2 distribution with n degrees of freedom [6].

This formulae can be rewritten into the form [7]

$$\chi^2 = \sum_{i=1}^{k} \frac{(n_i - E_i)^2}{E_i}, \tag{10.3}$$

where E_i denotes theoretical frequency of the i-class (bin). Distribution of multiplicities in individual bins is supposed to be the Poisson one [2]. Similar formula can be shown for testing of two data sample with above defined frequencies n_i and m_i

$$\chi^2 = \sum_{i=1}^{k} \frac{(n_i - m_i)^2}{m_i}. \tag{10.4}$$

This quantity is distributed according to the χ^2 distribution with $(k-1)$ degrees of freedom in the limit case $n \to \infty$. This is proven in [9].

The χ^2 test fails at the confidence level α if

$$\chi^2 \geq \chi^2_\alpha[k-1], \tag{10.5}$$

where $\chi^2_\alpha[k-1]$ is the χ^2 percent point function with $(k-1)$ degrees of freedom at confidence level α. Values of $\chi^2_\alpha[k-1]$ are defined that the

probability that a χ^2 random variable with $k-1$ degrees of freedom will exceed $\chi^2_\alpha[k-1]$ is α. These values are often called the critical values from the χ^2 distribution and are tabulated, e.g. [8].

It is necessary to consider several restrictions [7] for the χ^2 test application. The χ^2 test is applicable only in the cases when hypothetical frequencies $g_i \geq 1$ for all the classes and $g_i \geq 5$ for at least 80% of the classes. One general consequence of these restrictions is the synthesis of several classes with low frequencies at the ends of the tails of distributions.

10.2 Kolmogorov-Smirnov test

Kolmogorov-Smirnov (K-S) goodness of fit test is generally more powerful device for testing of hypotheses about the shape of random variable distribution than the χ^2 test. The K-S test can be used in case of low statistic data samples. The test does not work with the frequencies of classes but deals directly with values of measured data x_i, $i = 1, \ldots, n$. K-S test is based on a comparison of the empirical distribution function (EDF) $S_n()$ defined below. For that reason, K-S test is classed among EDF tests.

The main advantage of Kolmogorov-Smirnov test [38] is that the distribution of the K-S test statistic itself does not depend on the underlying distribution function being tested. Another advantage is that K-S test is exact and does not need any approximation. Despite, the K-S test can only by applied to continuous distributions.

At first it is needed to arrange the aggregate of data $x_1, \ldots, x_n$ according to a magnitude from lowest to highest value and resign at $x_{(1)}, \ldots, x_{(n)}$.

Second task is to evaluate a empirical distribution function $S_n(x)$, defined [7]

$$S_n(x) = \frac{i}{n}, \tag{10.6}$$

where i is the number of sample elements with values $\leq x$. Thus, $S_n(x)$ is a nondecreasing step function and has a jump of $\frac{1}{n}$ at each $x_{(i)}$. $S_n(x)$ is estimation of real cumulative distribution function of random variable X. In the case where measured data are stored in one dimensional histogram (the most frequently used form in analysis performed in programm ROOT), the empirical distribution is calculated from histogram bins.

Next step consists in the comparison of vertical distance between empirical distribution $S_n(x)$ and expected theoretical distribution $F(x)$. This maximum Kolmogorov distance is defined [7]

$$D = \max\{D^+, D^-\}, \tag{10.7}$$

where

$$D^+ = \sup_x\{S_n(x) - F(x)\} = \max_i\{\frac{i}{n} - F(x_i)\}, \tag{10.8}$$

$$D^- = \sup_x\{F(x) - S_n(x)\} = \max_i\{F(x_i) - \frac{i-1}{n}\}. \tag{10.9}$$

For two experimental empirical distribution functions $S_n(x)$ and $S_m(x)$ is maximum Kolmogorov distance defined in the following way [6]:

$$D = \max_x\{S_n(x) - S_m(x)\}. \tag{10.10}$$

The null-hypothesis about identical distributions is rejected at confidence level α if the maximum Kolmogorov distance fulfill [38]:

$$D > D_\alpha(n). \tag{10.11}$$

The number $D_\alpha(n)$ is called the critical value of the tested characteristics and it is tabulated [8].

Chapter 11

Analysis of generated events

The aim of this work is to compare distributions of kinematic quantities of Z boson and its secondaries created in interactions $pp \rightarrow X + Z \rightarrow e^+e^-$ at 14 TeV generated with several parton distribution function.

11.1 Files used for the analysis

Generators used for this analysis were HERWIG Version 6.507 [27] together with JIMMY Version 4.0 and PYTHIA Version 6.323 [28]. The full matrix element (including Z, γ, and interference term) was used during the generation. The minimum mass of the generated Z was set to the 60 GeV. Such steering parameters (see Appendix B) were chosen, so that programs generated inclusive collisions with unpolarized proton-proton at c. m. energy 14 TeV in initial state and the final state containing Z boson decaying into e^+e^- channel. The programs were used in the framework ATHENA of offline software Rel 11.0.41 of the experiment ATLAS [36].

The Les Houches Accord Parton Density Function (LHAPDF) Version 4.0 interface package [29] was used for implementation of sets of PDFs into generation. Many of PDF sets are available in this library. Five of them were chosen for this study. They are listed in Table 11.1 together with their codes and appropriate ranges for x and Q^2.

PDF set CTEQ6ll was used for the comparison between Herwig and Pythia. The main task, kinematic predictions for Z boson, was fulfilled by creation of below shown distributions of kinematic characteristics for Z and secondary electrons and positrons. Distributions of mass, transverse

Table 11.1: Proton PDFs selected for comparison.

PDF set	**code**	$\mathbf{x}_{min}$	$\mathbf{x}_{max}$	$\mathbf{Q}^2_{min}$	$\mathbf{Q}^2_{max}$
CTEQ6L	10041	10^{-6}	1	1.69	10^8
CTEQ6ll	10042	10^{-6}	1	1.69	10^8
CTEQ6m	10050	10^{-6}	1	1.69	10^8
MRST2004	20400	10^{-5}	1	1.25	10^7
ZEUS2005	60300	10^{-6}	1	0.3	2×10^5

momentum, rapidity and parton fraction momentum x_a were created.

11.2 Event selection, cuts, objects

Four event samples are defined for each generated set. No cut is used for the definition of the all events data sample. It is formed by all events (10^6) of the corresponding set.

The electron sample is created by the application of cuts to the secondary leptons. Events are accepted if electron has $p_T > 20$ GeV and $|\eta| < 2.5$. These cuts correspond to the acceptance region of the ATLAS detector [11]. The same cut is required for the secondary positrons and accepted events form positron sample.

The Z sample contains only events in which both secondary leptons survived the lepton cut. So, it is identical to the intersection of electron and positron samples.

The kinematic quantities of four types of objects are investigated in the rest of this chapter. By electrons and positrons are meant the Z secondaries obtained directly from the generator record. Z boson corresponds to the Z from the generator record. By lepton pair is meant fourmomentum constructed from the fourmomenta of electrons and positrons created by Z decay.

The generated sets were analyzed by object oriented data analysis framework ROOT Version 5.12/00 [24].

11.3 Expected multiplicities of Z boson

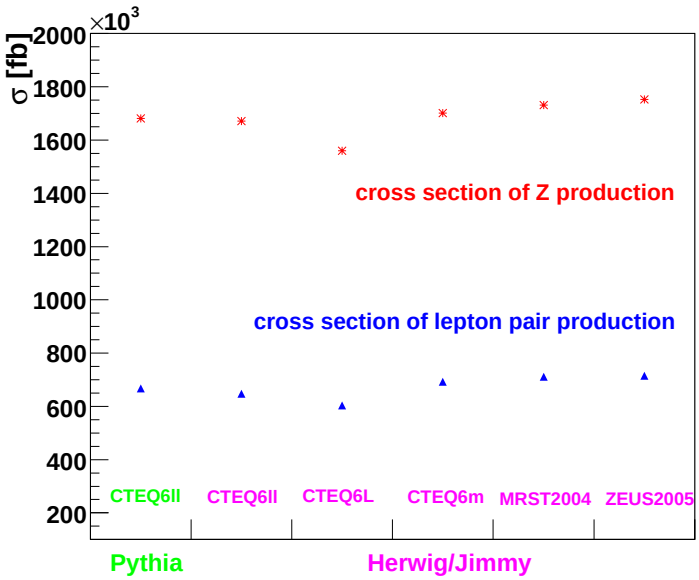

Figure 11.1: Graphical comparison of the cross sections for Z boson creation. The upper red set of points corresponds to Z production cross sections and the lower set corresponds to the cross section of Z sample.

Table 11.2 summarizes numbers of Z and cross sections for first and third event sample. It is possible to provide prediction for cross section of Z detection (last column in Table 11.2). The efficiency of lepton identification and detection is supposed to be 70% [11]. Neither other detector effects, nor background corrections are taken into account in this estimate. The PDF set ZEUS2005 embodies the most interesting properties. Via the final-state radiation by secondary leptons is cross section for lepton pair production reduced with respect to the large cross section of Z production.

Cross sections in Table 11.2 are drawn in Fig. 11.1. This dependence of cross sections on PDFs is responsible for different normalization of following kinematic distributions.

Table 11.2: Cross sections of Z production and of Z sample production for all selected PDFs for Pythia and Herwig/Jimmy generators.

	number of generated Z	**cross section [fb]**	**Relative fraction [%]**
Pythia			
CTEQ6ll	1,000,000	$1.681\ 10^6$	100.6
Herwig			
CTEQ6ll	1,000,000	$1.671\ 10^6 \pm 948.2$	100.0
CTEQ6L	1,000,000	$1.560\ 10^6 \pm 888.2$	93.4
CTEQ6m	1,000,000	$1.701\ 10^6 \pm 955.2$	101.8
MRST2004	1,000,000	$1.731\ 10^6 \pm 982.6$	103.6
ZEUS2005	1,000,000	$1.753\ 10^6 \pm 986.2$	104.9

	Z sample	**cross section [fb]**	**Relative fraction [%]**
Pythia			
CTEQ6ll	396,677	$0.667\ 10^6$	103.1
Herwig			
CTEQ6ll	387,457	$0.647\ 10^6$	100.0
CTEQ6L	386,739	$0.603\ 10^6$	93.2
CTEQ6m	407,347	$0.693\ 10^6$	107.1
MRST2004	410,713	$0.711\ 10^6$	109.9
ZEUS2005	407,654	$0.714\ 10^6$	110.4

	number of expected Z for detection	**cross section of Z detection [fb]**
Pythia		
CTEQ6ll	194,372	$0.327\ 10^6$
Herwig		
CTEQ6ll	189,854	$0.317\ 10^6$
CTEQ6L	189,502	$0.296\ 10^6$
CTEQ6m	199,600	$0.340\ 10^6$
MRST2004	201,249	$0.348\ 10^6$
ZEUS2005	199,750	$0.350\ 10^6$

11.4 P_T and η distributions for Z secondaries

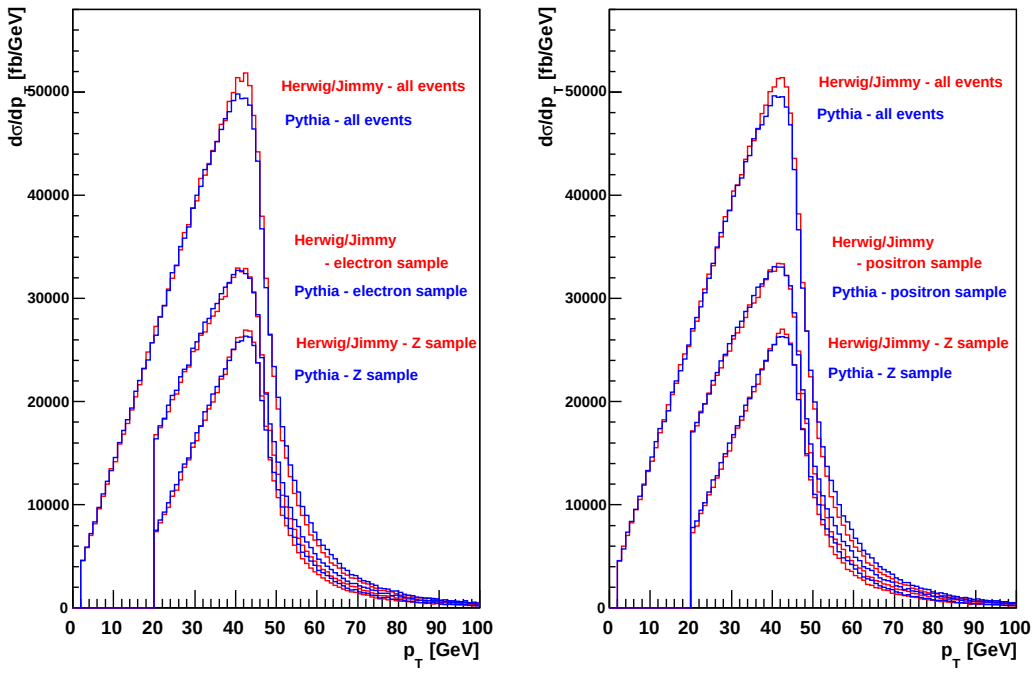

Figure 11.2: Differential cross section as a function of transverse momentum of electrons (on the left) and positrons (on the right). CTEQ6ll parton distribution function was used for both generators.

There is a comparison of p_T distributions between Herwig/Jimmy and Pythia for both electrons and positrons for all three event samples in Fig. 11.2. The influence of the lepton cut can be perfectly seen at $20GeV$. There is remarkable difference between Pythia and Herwig/Jimmy, especially for all events. There is no obvious difference between electrons and positrons. The comparison of p_T distributions for electrons from Z sample for different PDFs for Herwig/Jimmy generator is shown in Fig. 11.3. Distributions differ in normalization, see Fig. 11.1.

There is a distinct difference between Herwig and Pythia generators in Fig. 11.4, which survived all cuts. Herwig distributions are significantly

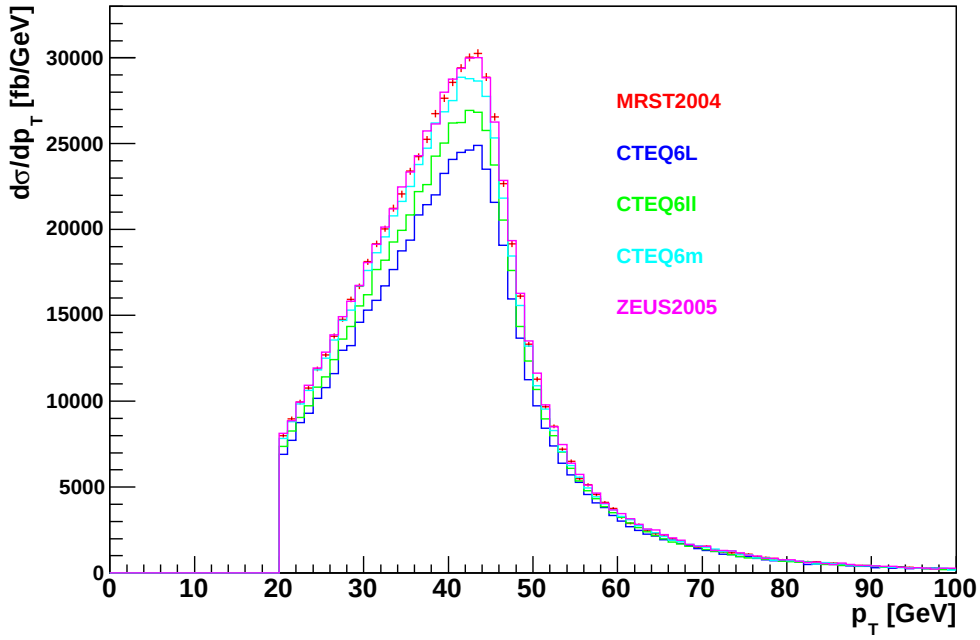

Figure 11.3: Differential cross section as a function of transverse momentum of electrons from Z sample. Five PDF sets are compared. The distributions for positrons are almost identical.

wider. The effect of $|\eta| < 2.5$ cut can be well seen. The last cut causes significant change in the shape of distribution.

The pseudorapidity distributions of electron are shown in Fig. 11.5 for five PDFs.

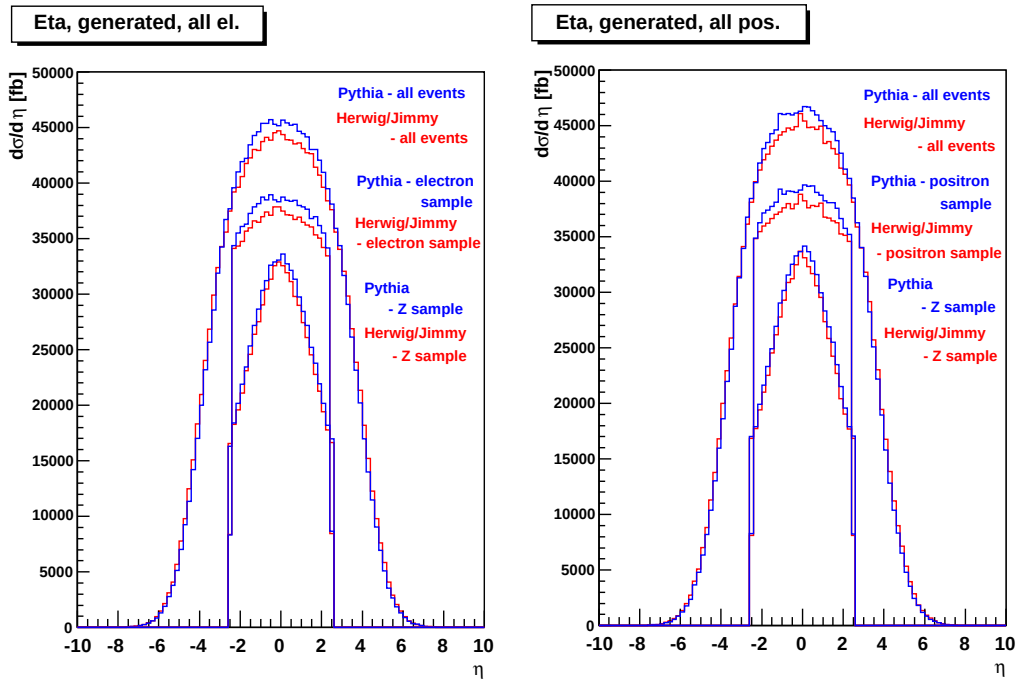

Figure 11.4: Differential cross section as a function of pseudorapidity of electrons (on the left) and positrons (on the right). CTEQ6ll parton distribution function was used for both generators.

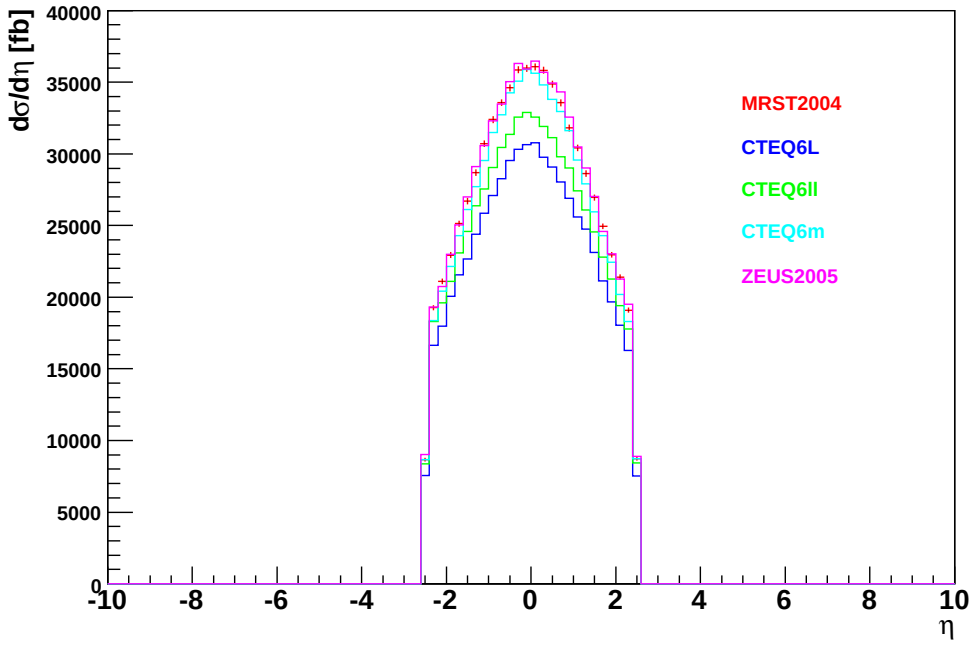

Figure 11.5: Differential cross section as a function of pseudorapidity of electrons from Z sample. Five PDF sets are compared. The distributions for positrons are almost identical.

11.5 Kinematic characteristics of Z boson

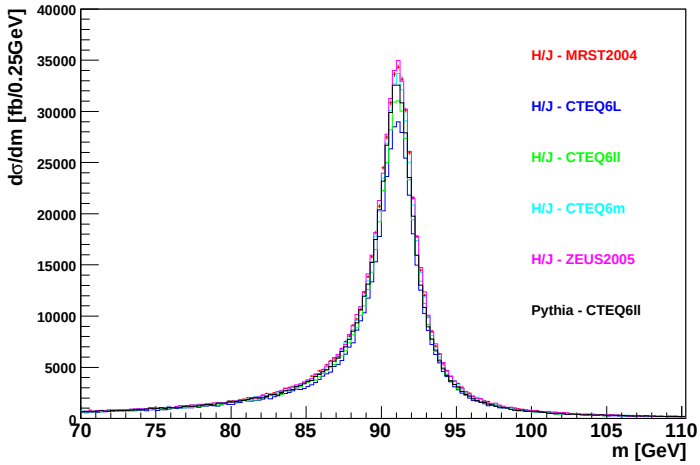

Figure 11.6: Differential cross section as a function of invariant mass of the lepton pair from Z sample for five PDFs using different generators.

The mass distributions of the lepton pair from Z sample for all PDFs are shown in Fig. 11.6. Shape of the distributions is almost identical with respect to the normalization, see Fig. 11.1.

The p_T distributions of Z boson and lepton pair are shown in the Fig. 11.7 for CTEQ6ll PDF for Herwig and Pythia. There is very strong difference between them. Herwig predicts higher cross sections in the area of $p_T < 15$ GeV compared to Pythia and vice versa in the area of $p_T > 15$ GeV.

The comparison of distributions obtained with different PDFs (Herwig/Jimmy) is shown in Fig. 11.8. They differ in normalization, see Fig. 11.1.

Fig. 11.9 shows rapidity distributions for CTEQ6ll PDF using Herwig and Pythia generator. Herwig predicts slightly wider peaks.

The comparison of rapidity distributions of lepton pair from Z sample for all sets of PDFs using Herwig generator is displayed in Fig. 11.10. Differences are in normalization.

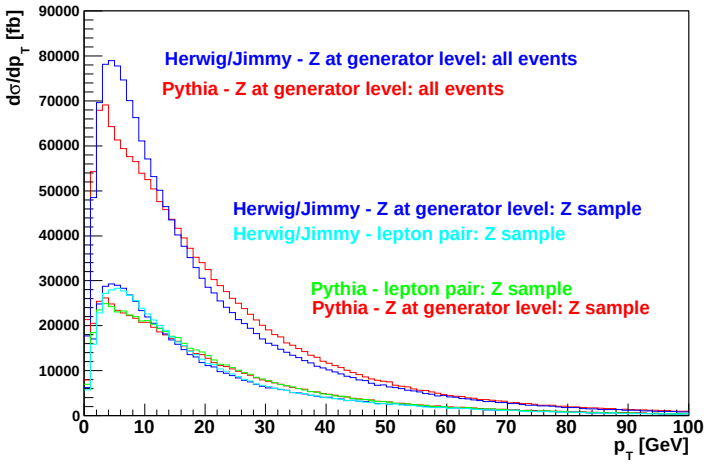

Figure 11.7: Differential cross section as a function of transverse momentum of Z boson and lepton pair. CTEQ6ll PDF was used for different generators.

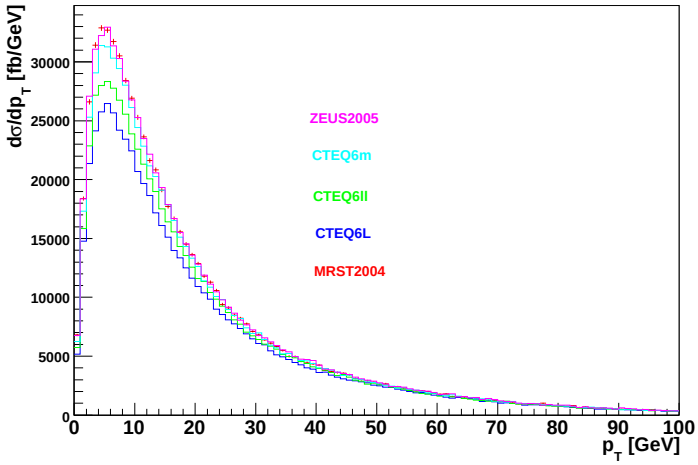

Figure 11.8: Differential cross section as a function of transverse momentum of the lepton pair from Z sample for different PDFs using Herwig/Jimmy generator.

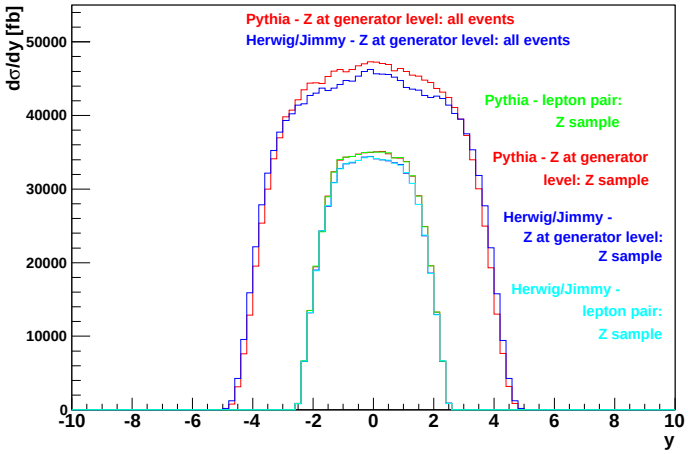

Figure 11.9: Differential cross section as a function of rapidity of Z boson and lepton pair for CTEQ6ll PDF using Herwig/Jimmy and Pythia generators.

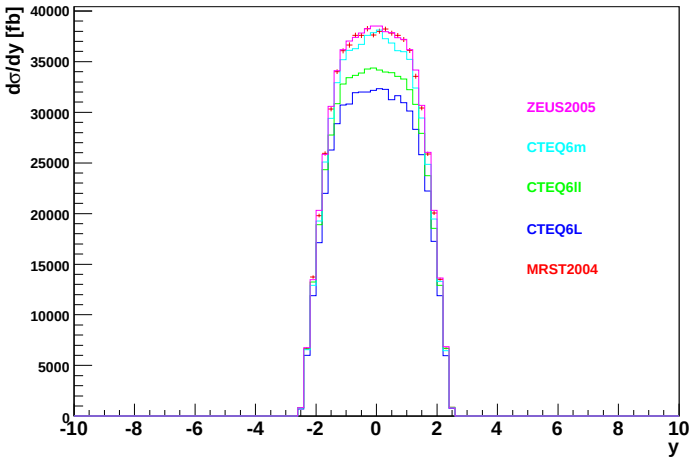

Figure 11.10: Differential cross section as a function of rapidity of the lepton pair from Z sample for different PDFs using Herwig/Jimmy generator.

11.6 Comparison of the Z boson mass distributions

The distributions of invariant mass of Z boson and lepton pair are investigated in this section. The range of invariant mass is $< 60.0, 200.0) GeV$

Tests described in Chapter 10 are theoretical solutions of the problem with comparison of two distributions of measured data. The program ROOT version 5.12/00 [37] is used in this study for quantitative analysis. Both tests are implemented as methods of the class of one dimensional histograms TH1.

The χ^2 test for binned data is implemented in ROOT as a function: Double_t Chi2Test(const TH1 *h, Option_t *option, Int_t constraint)[43] of the class of one-dimensional histograms TH1. The data storing in histograms perfectly suits the χ^2 test [43] because this test deals with the frequencies of the above defined classes. At the first sight it is natural use this test for its simplicity but there is one main parameter which changes results of the test. This is binnig. The results of the χ^2 test for all three event samples are listed in Tables A.1-A.12. These tables differ in number of bins and event sample used for filling of histograms. The dependencies of probabilities on binning are shown in Fig.11.12, 11.14, and 11.16. All histograms are normalized to number of events contained in histogram for Herwig/Jimmy CTEQ6ll in corresponding event sample.

The Kolmogorov-Smirnov test for binned data is implemented in ROOT as a function: Double_t KolmogorovTest(const TH1 *h2, Option_t *option)[42] of the class of one-dimensional histograms TH1. The empirical distribution function can be extracted from data stored in histograms as described in Chapter 10. The results of K-S test are listed in Tables A.1-A.12. These tables differ in number of bins and in data sample used for filling of histograms. The dependencies of probabilities on binning are shown in Fig.11.11, 11.13, and 11.15. The dependence on binning is generally very low.

The main problem for both tests dealing with binned data is the width of the bin. The manual of program ROOT [42] advises to apply a rule: "As long as the bin width is small compared with any significant physical effect (for example the experimental resolution) then the binning cannot have an important effect". For that reason the biggest number of bins from bin-dependence graph (e.g. 11.11) is used for further analysis.

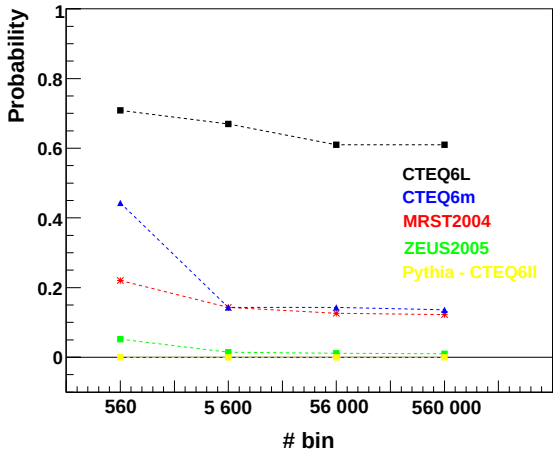

Figure 11.11: Dependence of the probabilities of distribution consistency for several PDFs from Kolmogorov-Smirnov test on number of bins for Z boson (all events). The reference distributions were created from event sets generated by Herwig/Jimmy with CTEQ6ll.

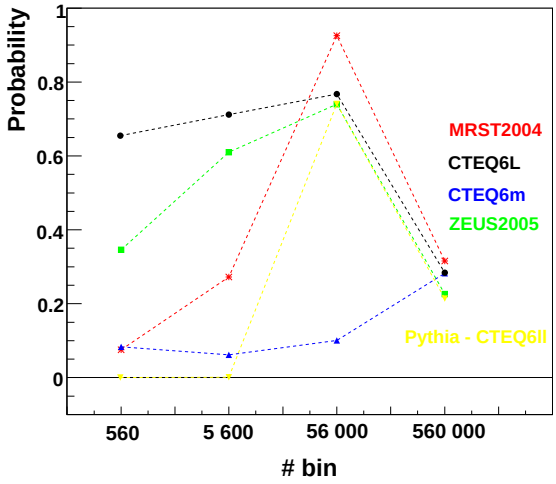

Figure 11.12: Dependence of the probabilities of distribution consistency for several PDFs from χ^2 test on number of bins for Z boson (all events). The reference distributions were created from event sets generated by Herwig/Jimmy with CTEQ6ll.

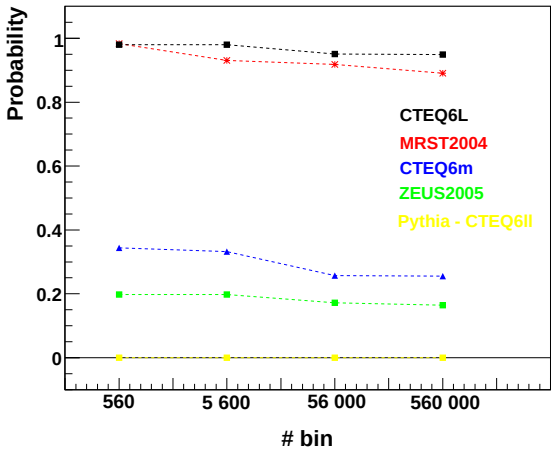

Figure 11.13: Dependence of the probabilities of distribution consistency for several PDFs from Kolmogorov-Smirnov test on number of bins for Z boson (Z sample). The reference distributions were created from event sets generated by Herwig/Jimmy with CTEQ6ll.

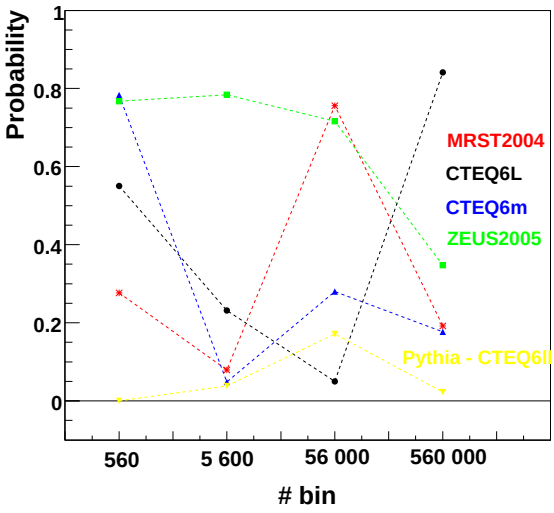

Figure 11.14: Dependence of the probabilities of distribution consistency for several PDFs from χ^2 test on number of bins for Z boson (Z sample). The reference distributions were created from event sets generated by Herwig/Jimmy with CTEQ6ll.

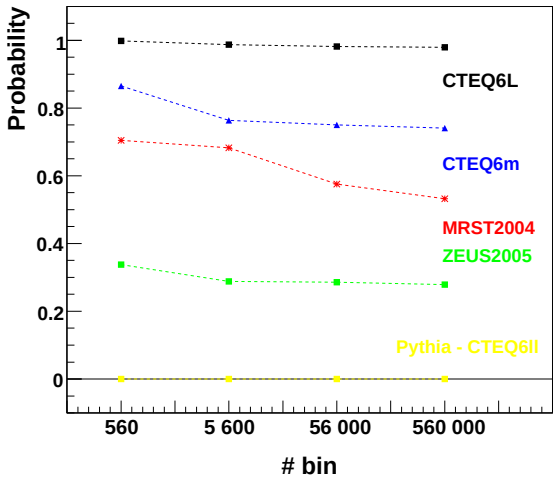

Figure 11.15: Dependence of the probabilities of distribution consistency for several PDFs from Kolmogorov-Smirnov test on number of bins for lepton pair (Z sample). The reference distributions were created from event sets generated by Herwig/Jimmy with CTEQ6ll.

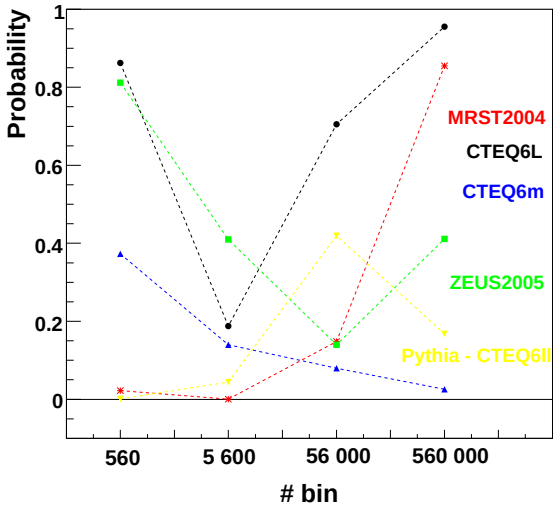

Figure 11.16: Dependence of the probabilities of distribution consistency for several PDFs from χ^2 test on number of bins for lepton pair (Z sample). The reference distributions were created from event sets generated by Herwig/Jimmy with CTEQ6ll.

There were prepared a lot of probabilities of Z boson mass distribution consistency in this section: for two data samples, and for four histogram binnings. As the results shows, the χ^2 test is very sensitive to the binning of histograms. The results of Kolmogorov-Smirnov embody very low dependance on histogram binning.

The result of this investigation is that Kolmogorov-Smirnov test implemented as a function of the class of one dimensional histograms in program ROOT v. 5.12/00 will be used for the comparison of other kinematic variables of Z boson investigated in this study.

11.7 P_T, η, and rapidity distributions of electron and lepton pair - dependence of probability on binning for K-S test

It was shown in the previous section that there is a small dependence of the probability calculated via Kolmogorov-Smirnov test on the used binning of the x-axis of the histograms. The probability slightly decreases with increased number of bins, as expected. The higher number of bins is used the less is the effect of binning.

The comparison of histogram consistency for CTEQ6L and CTEQ6ll PDF from Herwig/Jimmy for four different binnings of histograms of different variables of electrons and lepton pairs from Z sample is presented. The results are listed in Tables 11.3, 11.4 and graphically shown in Fig.11.17, 11.18. The interval $< 0.0, 100.0)GeV$ of p_T ($< -6.0, 6.0$) of rapidity) is taken into account for lepton pair. The interval $< 20.0, 100.0)GeV$ of p_T ($< -3.0, 3.0$) of pseudorapidity) is taken into account for electron. Z sample is investigated in both cases.

Similarly as in the case of invariant mass distributions, the dependence of probability of K-S test is very low for all investigated distributions.

Table 11.3: Probabilities and maximum distances for electron (Z sample) p_T and η distributions using K-S test. Distributions obtained with CTEQ6ll and CTEQ6L are tested. Herwig/Jimmy generator was used.

number of bins	**p_T distributions**	
	probability	**max. distance**
800	0.0069	0.0038
8 000	0.0069	0.0038
80 000	0.0068	0.0039
800 000	0.0068	0.0039
number of bins	**pseudorapidity distributions**	
	probability	**max. distance**
600	0.4154	0.0020
6 000	0.3959	0.0020
60 000	0.3910	0.0021
600 000	0.3878	0.0021

Table 11.4: Probabilities and maximum distances for lepton pair (Z sample) p_T and y distributions using K-S test. Distributions obtained with CTEQ6ll and CTEQ6L are tested. Herwig/Jimmy generator was used.

number of bins	**p_T distributions**	
	probability	**max. distance**
1 000	$3.1\ 10^{-10}$	0.0077
10 000	$2.9\ 10^{-10}$	0.0077
100 000	$2.5\ 10^{-10}$	0.0078
1 000 000	$2.5\ 10^{-10}$	0.0078
number of bins	**rapidity distributions**	
	probability	**max. distance**
1 200	0.0265	0.0033
12 000	0.0228	0.0034
120 000	0.0226	0.0034
1 200 000	0.0226	0.0034

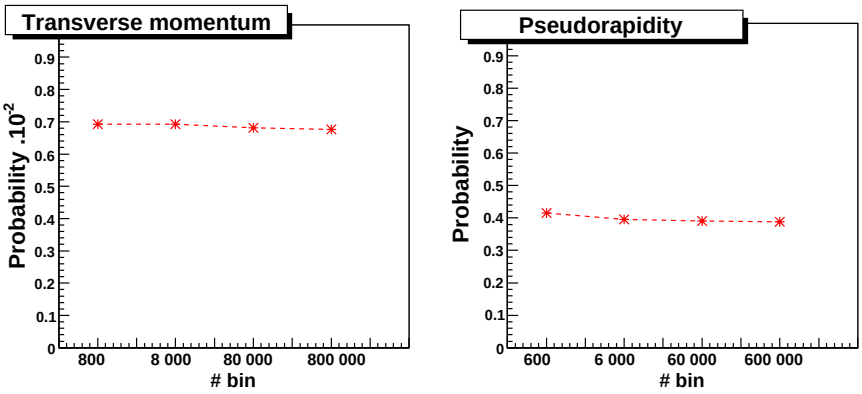

Figure 11.17: Dependence of the probabilities of distribution consistency for CTEQ6L and CTEQ6ll PDFs from Kolmogorov-Smirnov test on number of bins for the electrons - Z sample.

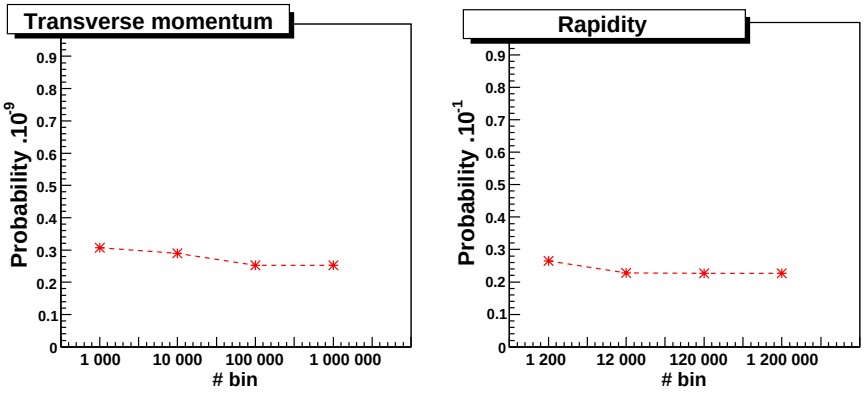

Figure 11.18: Dependence of the probabilities of distribution consistency for CTEQ6L and CTEQ6ll PDFs from Kolmogorov-Smirnov test on number of bins for the lepton pairs - Z sample.

11.8 Results of the Kolmogorov-Smirnov test

In this Section are numerically compared the most important distributions of kinematical variables of Z and its secondaries shown in the Sections 11.4 and 11.5. The Kolmogorov-Smirnov test implemented in ROOT 5.12/00 [37] was used for calculation.

There were compared the p_T and pseudorapidity distributions of electrons and positrons from Z sample. The range $< 20.0, 100.0)GeV$ of p_T divided into 800 000 bins was taken into account. The used interval $< -3.0, 3.0)$ of pseudorapidity was divided into 600 000 bins. Distributions obtained with CTEQ6ll (Herwig/Jimmy) were used as reference distributions. The probabilities of consistency as well the maximum Kolmogorov distances for all PDFs and both generators are summarized in Tables 11.5, 11.6. These Tables correspond to the Fig. 11.19, 11.20.

There were compared the mass, p_T, and rapidity distributions of Z boson and lepton pair. The mass distribution is divided into 560 000 bins in the range $< 60.0, 200.0)GeV$, because $60.0GeV$ was the minimum mass of Z set in steering of generation. The range $< 0.0, 100.0)GeV$ of p_T divided into 1 000 000 bins was taken into account. The used interval $< -6.0, 6.0)$ of pseudorapidity was divided into 1 200 000 bins. Distributions obtained with CTEQ6ll (Herwig/Jimmy) were used as reference distributions. The probabilities of consistency as well as the maximum Kolmogorov distances for mass distributions for all PDFs and both generators are recapitulated in Table 11.7. Fig.11.21 is the graphical representation of probabilities from Table 11.7. The results (probabilities and maximal distances) for p_T distributions are summarized in Table 11.8. This Table corresponds to the Fig.11.22, where maximal distances are drawn instead of probabilities. The comparison of rapidity distributions are listed in Table 11.9 and the probabilities are drawn in Fig.11.23.

Table 11.5: Probabilities and maximum distances for p_T and pseudorapidity distributions of electrons from Z sample using K-S test. The reference distributions were created from event sets generated by Herwig/Jimmy with CTEQ6ll.

	p_T **distributions**		η **distributions**	
PDF	**probability**	**max. dist.**	**probability**	**max. dist.**
Pythia CTEQ6ll Herwig				
CTEQ6L	0.0068	0.0039	0.3878	0.0021
CTEQ6m	0.0003	0.0047	$1.6\ 10^{-5}$	0.0054
MRST2004	$1.0\ 10^{-6}$	0.0061	0.0013	0.0043
ZEUS2005	0.0113	0.0036	0.0015	0.0043

Table 11.6: Probabilities and maximum distances for p_T and pseudorapidity distributions of positrons from Z sample using K-S test. The reference distributions were created from event sets generated by Herwig/Jimmy with CTEQ6ll.

	p_T **distributions**		η **distributions**	
PDF	**probability**	**max. dist.**	**probability**	**max. dist.**
Pythia CTEQ6ll Herwig				
CTEQ6L	0.1105	0.0027	0.1708	0.0025
CTEQ6m	$2.4\ 10^{-5}$	0.0054	$1.9\ 10^{-5}$	0.0054
MRST2004	$3.1\ 10^{-7}$	0.0063	0.0015	0.0043
ZEUS2005	$2.7\ 10^{-9}$	0.0072	0.0001	0.0049

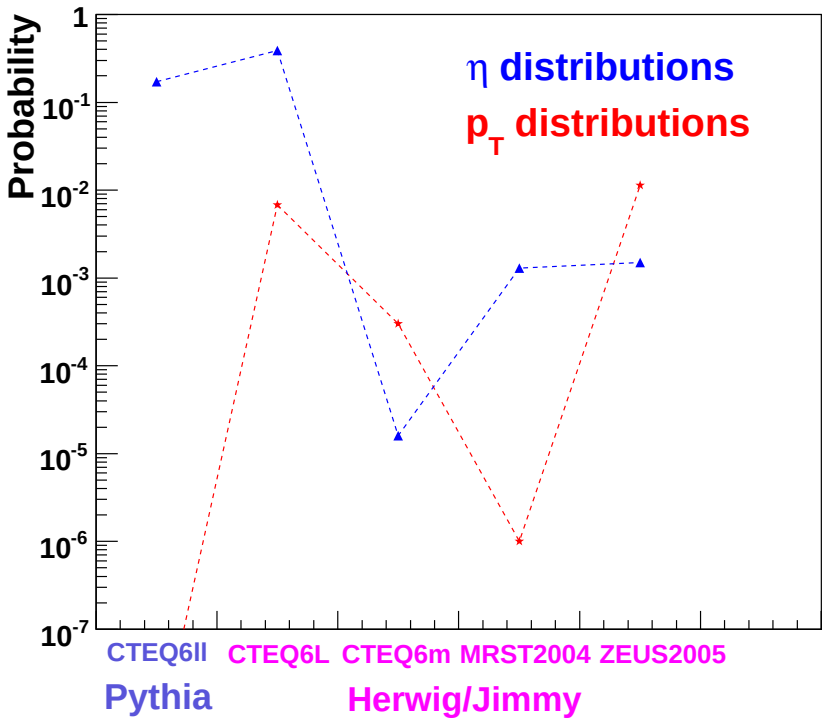

Figure 11.19: Probabilities for p_T and pseudorapidity distributions of electrons from Z sample using K-S test. The reference distributions were created from event sets generated by Herwig/Jimmy with CTEQ6ll.

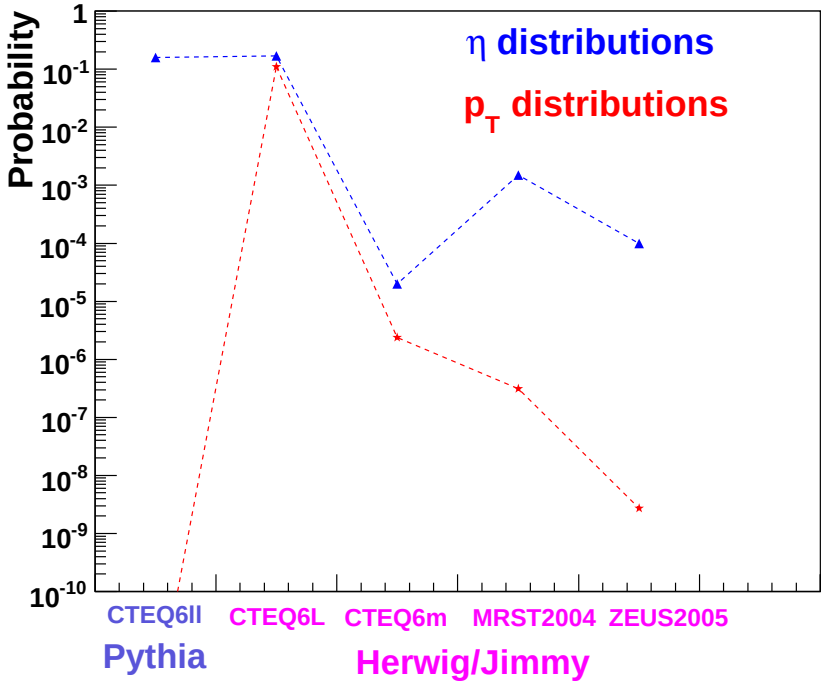

Figure 11.20: Probabilities for p_T and pseudorapidity distributions of positrons from Z sample using K-S test. The reference distributions were created from event sets generated by Herwig/Jimmy with CTEQ6ll.

Table 11.7: Probabilities and maximum distances for Z boson and lepton pair mass distributions using K-S test. The reference distributions were created from event sets generated by Herwig/Jimmy with CTEQ6ll.

	Z at generator level - all events	
PDF	**probability**	**max. distance**
Pythia		
CTEQ6ll	0.0000	0.0119
Herwig		
CTEQ6L	0.6099	0.0011
CTEQ6m	0.1365	0.0016
MRST2004	0.1222	0.0017
ZEUS2005	0.0100	0.0023

	Z at generator level - Z sample	
PDF	**probability**	**max. distance**
Pythia		
CTEQ6ll	$7.2\ 10^{-37}$	0.0146
Herwig		
CTEQ6L	0.9487	0.0012
CTEQ6m	0.2554	0.0023
MRST2004	0.8903	0.0013
ZEUS2005	0.1645	0.0025

	lepton pair - Z sample	
PDF	**probability**	**max. distance**
Pythia		
CTEQ6ll	$1.6\ 10^{-20}$	0.0109
Herwig		
CTEQ6L	0.9791	0.0011
CTEQ6m	0.7408	0.0015
MRST2004	0.5321	0.0018
ZEUS2005	0.2790	0.0022

Table 11.8: Probabilities and maximum distances for Z boson and lepton pair p_T distributions using K-S test. The reference distributions were created from event sets generated by Herwig/Jimmy with CTEQ6ll.

	Z at generator level - all events	
PDF	**probability**	**max. distance**
Pythia		
CTEQ6ll	0.0000	0.0549
Herwig		
CTEQ6L	$8.0\ 10^{-25}$	0.0076
CTEQ6m	0.0000	0.0112
MRST2004	0.0000	0.0193
ZEUS2005	0.0000	0.0180

	Z at generator level - Z sample	
PDF	**probability**	**max. distance**
Pythia		
CTEQ6ll	0.0000	0.0543
Herwig		
CTEQ6L	$2.0\ 10^{-10}$	0.0078
CTEQ6m	$1.0\ 10^{-19}$	0.0107
MRST2004	0.0000	0.0192
ZEUS2005	$4.9\ 10^{-38}$	0.0149

	lepton pair - Z sample	
PDF	**probability**	**max. distance**
Pythia		
CTEQ6ll	0.0000	0.0526
Herwig		
CTEQ6L	$2.5\ 10^{-10}$	0.0078
CTEQ6m	$2.1\ 10^{-17}$	0.0100
MRST2004	0.0000	0.0178
ZEUS2005	$1.4\ 10^{-33}$	0.0140

Table 11.9: Probabilities and maximum distances for Z boson and lepton pair rapidity distributions using K-S test. The reference distributions were created from event sets generated by Herwig/Jimmy with CTEQ6ll.

	Z at generator level - all events	
PDF	**probability**	**max. distance**
Pythia		
CTEQ6ll	0.0000	0.0101
Herwig		
CTEQ6L	0.1229	0.0017
CTEQ6m	0.0000	0.0146
MRST2004	0.0000	0.0164
ZEUS2005	0.0000	0.0147

	Z at generator level - Z sample	
PDF	**probability**	**max. distance**
Pythia		
CTEQ6ll	0.1206	0.0027
Herwig		
CTEQ6L	0.0248	0.0034
CTEQ6m	$1.3\ 10^{-7}$	0.0065
MRST2004	$1.3\ 10^{-4}$	0.0049
ZEUS2005	$4.4\ 10^{-5}$	0.0052

	lepton pair - Z sample	
PDF	**probability**	**max. distance**
Pythia		
CTEQ6ll	0.1055	0.0027
Herwig		
CTEQ6L	0.0226	0.0034
CTEQ6m	$1.2\ 10^{-7}$	0.0065
MRST2004	$1.2\ 10^{-4}$	0.0049
ZEUS2005	$3.5\ 10^{-5}$	0.0052

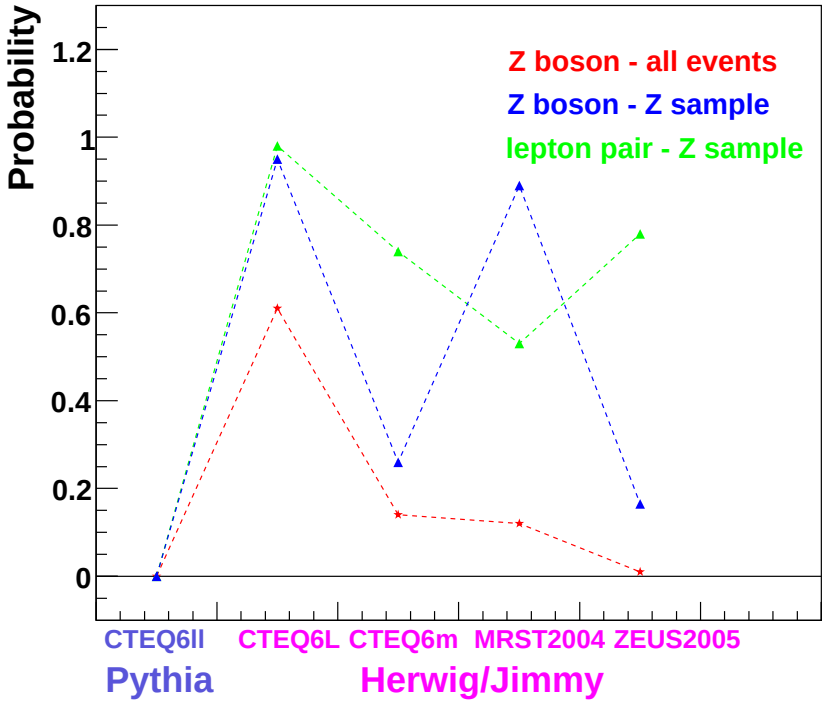

Figure 11.21: Probabilities for Z boson and lepton pair mass distributions using K-S test. The reference distributions were created from event sets generated by Herwig/Jimmy with CTEQ6ll.

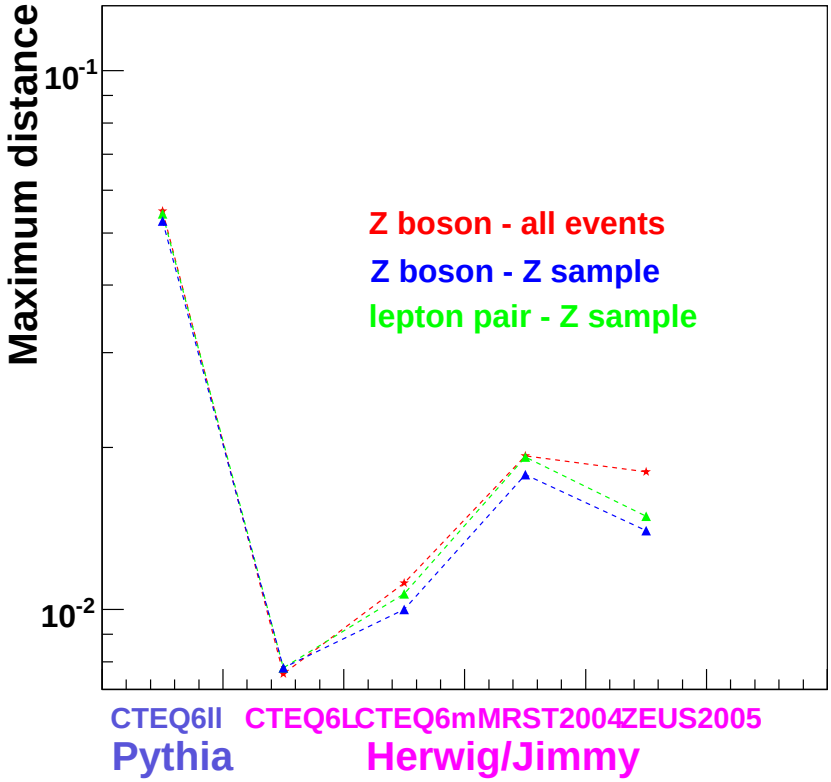

Figure 11.22: Maximum Kolmogorov distancies for Z boson and lepton pair p_T distributions using K-S test. The graph of probabilities is not shown, because all probabilities of consistency are very close to 0%. The reference distributions were created from event sets generated by Herwig/Jimmy with CTEQ6ll.

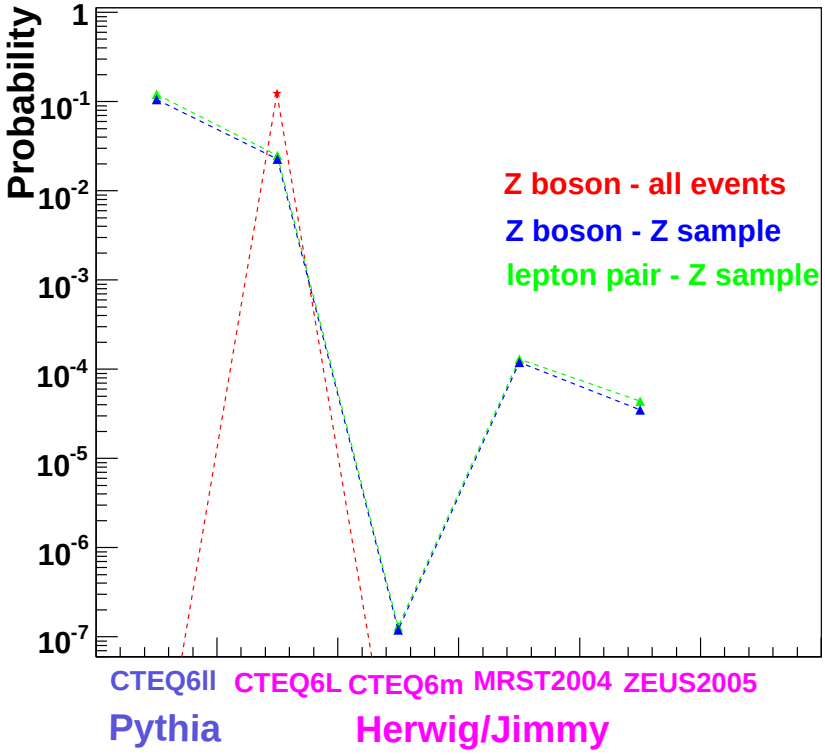

Figure 11.23: Probabilities for Z boson and lepton pair rapidity distributions using K-S test. The reference distributions were created from event sets generated by Herwig/Jimmy with CTEQ6ll.

Chapter 12

Summary and conclusions

Kinematic characteristics of Z boson and its secondaries created in the process $pp \rightarrow X + Z \rightarrow e^- e^+$ at 14 TeV were studied on the generator level. Two generators were used: Herwig/Jimmy and Pythia. Five different event sets were generated with Herwig/Jimmy. They differ only in PDF. The following PDFs were used: CTEQ6ll (used also in Pythia), CTEQ6L, CTEQ6m, MRST2004 and ZEUS2005. The first three are leading order PDFs, the last two are next-to-leading order ones.

The expected multiplicity of Z boson decayed in $e^- e^+$ channel are 3.27×10^5, 10^6, 10^7 for the integrated luminosity 1, 10 and 100 fb^{-1}, respectively for events generated with Pythia. These numbers differ from 3.17×10^5, 10^6, 10^7 generated with Herwig/Jimmy using the same PDF set by about 3.2%. The identification and reconstruction efficiency is supposed to be 70 % for the electrons and positrons with $p_T > 20GeV$ and $|\eta| < 2.5$. Other detector effects and background corrections are not taken into account.

Herwig/Jimmy event generator was used for comparison of different sets of PDFs. The expected multiplicities are 2.96×10^5, 3.17×10^5, 3.40×10^5, 3.48×10^5 and 3.50×10^5 for integrated luminosity 1 fb^{-1}. They correspond to CTEQ6L, CTEQ6ll, CTEQ6m, MRST2004 and ZEUS2005 PDF sets.

Two different tests were investigated for the purpose of comparison of distributions of kinematic quantities of Z boson and its secondaries: χ^2 test and Kolmogorov-Smirnov test for binned data. Because of its weak dependence on the histogram binning (Chapters 11.6 and 11.7) Kolmogorov-Smirnov test was chosen. The confidence level for considering that two distributions are identical was set to 95.0%.

Distributions obtained with CTEQ6ll PDF (Herwig/Jimmy) were used

as reference distributions. Distributions obtained with other PDFs were normalized to the same number of events.

The consistencies of distributions of transverse momentum and pseudorapidity for electrons and positrons from Z sample were investigated. Results are summarized in Tables 11.5, 11.6. All distributions are found not to be identical with the reference one. The most similar distribution of p_T of electron to the reference one is distribution obtained by ZEUS2005 PDF (Herwig/Jimmy). The confidence level of their consistency is 1.1%. The highest value of confidence level for consistency of p_T distributions for positron with reference distribution is 11.1% for distribution obtained with CTEQ6L PDF (Herwig/Jimmy). The most similar distribution of pseudorapidity of electron with the reference one is distribution obtained by CTEQ6L PDF (Herwig/Jimmy). The confidence level of their consistency is 38.8%. The highest value of confidence level for consistency of pseudorapidity distributions for positron with reference distribution is 17.1% for distribution obtained with CTEQ6L PDF (Herwig/Jimmy). The distributions obtained from Pythia and Herwig are consistent at confidence level of 17.2% for electrons and of 15.9% for positrons.

The consistencies of distributions of mass, transverse momentum, and rapidity for Z boson and lepton pair were investigated. Results are listed in Tables 11.7,11.8, 11.9. The confidence levels of consistency of mass distributions obtained by different PDFs (Herwig/Jimmy) with the reference one are generally very high - in tenths of percent, except ZEUS2005 PDF for Z bosons from all events sample. The mass distributions of lepton pair from Z sample obtained with CTEQ6ll and CTEQ6L are identical. All other distributions are not identical with the reference one. Distributions of p_T of Z boson and lepton pair are not identical with the reference distributions. Values of confidence level are close to 0.0%. Distributions of rapidity of Z boson and lepton pair are not identical with the reference ones. Only distributions obtained with CTEQ6L have remarkable non-zero values of confidence level. The highest value is 12.3%. Distributions obtained from Pythia and Herwig are consistent at confidence level of 12.1% for Z boson from Z sample and of 10.6% for lepton pairs from Z sample.

The summary conclusions from this work are following. The values of the total cross section of investigated process $pp \to X + Z \to e^- e^+$ at 14 TeV differ by less than 5% from the cross section obtained with CTEQ6ll PDF for the investigated PDFs: CTEQ6L, CTEQ6ll, CTEQ6m, MRST2004, and ZEUS2005. These differences rise up to 10% when kinematic cuts cor-

responding to the acceptance region of ATLAS detector are applied to the Z boson secondaries. Shapes of all investigated distributions are found not to be identical with reference distributions at confidence level of 95.0% except lepton pair mass distribution obtained with CTEQ6L PDF (Herwig/Jimmy).

Appendix A

Comparison of the Z boson mass distributions

Table A.1: Probabilities and maximum distances (resp. χ^2/ndf) for Z boson (all events) mass distributions using K-S test (resp. χ^2 test). The reference distributions were created from event sets generated by Herwig/Jimmy with CTEQ6ll. The number of bins is 560 in the range of $< 60.0 - 200.0) GeV$.

	Kolmogorov-Smirnov test		χ^2 **test**	
PDF	**probability**	**max. distance**	**probability**	χ^2/ndf
Pythia				
CTEQ6ll	0.0000	0.0118	0.0000	1.7156
Herwig				
CTEQ6ll	1.0000	0.0000	1.0000	0.0000
CTEQ6L	0.7084	0.0010	0.6545	0.9752
CTEQ6m	0.4432	0.0012	0.0832	1.0838
MRST2004	0.2207	0.0015	0.0757	1.0870
ZEUS2005	0.0519	0.0019	0.3459	1.0227

Table A.2: Probabilities and maximum distances (resp. χ^2/ndf) for Z boson (all events) mass distributions using K-S test (resp. χ^2 test). The reference distributions were created from event sets generated by Herwig/Jimmy with CTEQ6ll. The number of bins is 5 600 in the range of $< 60.0 - 200.0) GeV$.

	Kolmogorov-Smirnov test		χ^2 **test**	
PDF	**probability**	**max. distance**	**probability**	χ^2/ndf
Pythia				
CTEQ6ll	0.0000	0.0118	0.0012	1.0593
Herwig				
CTEQ6ll	1.0000	0.0000	1.0000	0.0000
CTEQ6L	0.6696	0.0010	0.7121	0.9895
CTEQ6m	0.1429	0.0016	0.0617	1.0298
MRST2004	0.1428	0.0016	0.2722	1.0116
ZEUS2005	0.0141	0.0022	0.6099	0.9953

Table A.3: Probabilities and maximum distances (resp. χ^2/ndf) for Z boson (all events) mass distributions using K-S test (resp. χ^2 test). The reference distributions were created from event sets generated by Herwig/Jimmy with CTEQ6ll. The number of bins is 56 000 in the range of $< 60.0 - 200.0) GeV$.

	Kolmogorov-Smirnov test		χ^2 **test**	
PDF	**probability**	**max. distance**	**probability**	χ^2/ndf
Pythia				
CTEQ6ll	0.0000	0.0119	0.7407	0.9991
Herwig				
CTEQ6ll	1.0000	0.0000	1.0000	0.0000
CTEQ6L	0.6099	0.0011	0.7671	0.9977
CTEQ6m	0.1429	0.0016	0.1007	1.0095
MRST2004	0.1264	0.0017	0.9257	0.9903
ZEUS2005	0.0112	0.0023	0.7397	0.9992

Table A.4: Probabilities and maximum distances (resp. χ^2/ndf) for Z boson (all events) mass distributions using K-S test (resp. χ^2 test). The reference distributions were created from event sets generated by Herwig/Jimmy with CTEQ6ll. The number of bins is 560 000 in the range of $< 60.0 - 200.0) GeV$.

	Kolmogorov-Smirnov test		χ^2 **test**	
PDF	**probability**	**max. distance**	**probability**	χ^2/ndf
Pythia				
CTEQ6ll	0.0000	0.0119	0.2142	1.0026
Herwig				
CTEQ6ll	1.0000	0.0000	1.0000	0.0000
CTEQ6L	0.6099	0.0011	0.2836	1.0019
CTEQ6m	0.1365	0.0016	0.2826	1.0019
MRST2004	0.1222	0.0017	0.3160	1.0016
ZEUS2005	0.0100	0.0023	0.2262	1.0025

Table A.5: Probabilities and maximum distances (resp. χ^2/ndf) for Z boson (Z sample) mass distributions using K-S test (resp. χ^2 test). The reference distributions were created from event sets generated by Herwig/Jimmy with CTEQ6ll. The number of bins is 560 in the range of $< 60.0 - 200.0) GeV$.

	Kolmogorov-Smirnov test		χ^2 **test**	
PDF	**probability**	**max. distance**	**probability**	χ^2/ndf
Pythia				
CTEQ6ll	0.0000	0.0142	0.0000	1.4022
Herwig				
CTEQ6ll	1.0000	0.0000	1.0000	0.0000
CTEQ6L	0.9798	0.0011	0.5505	0.9912
CTEQ6m	0.3439	0.0021	0.7830	0.9528
MRST2004	0.9834	0.0010	0.2764	1.0347
ZEUS2005	0.1974	0.0024	0.7676	0.9558

Table A.6: Probabilities and maximum distances (resp. χ^2/ndf) for Z boson (Z sample) mass distributions using K-S test (resp. χ^2 test). The reference distributions were created from event sets generated by Herwig/Jimmy with CTEQ6ll. The number of bins is 5 600 in the range of $< 60.0 - 200.0) GeV$.

	Kolmogorov-Smirnov test		χ^2 **test**	
PDF	**probability**	**max. distance**	**probability**	χ^2/ndf
Pythia				
CTEQ6ll	0.0000	0.0145	0.0381	1.0356
Herwig				
CTEQ6ll	1.0000	0.0000	1.0000	0.0000
CTEQ6L	0.9798	0.0011	0.2318	1.0146
CTEQ6m	0.3319	0.0021	0.0487	1.0331
MRST2004	0.9309	0.0012	0.0793	1.0281
ZEUS2005	0.1974	0.0024	0.7838	0.9846

Table A.7: Probabilities and maximum distances (resp. χ^2/ndf) for Z boson (Z sample) mass distributions using K-S test (resp. χ^2 test). The reference distributions were created from event sets generated by Herwig/Jimmy with CTEQ6ll. The number of bins is 56 000 in the range of $< 60.0 - 200.0) GeV$.

	Kolmogorov-Smirnov test		χ^2 **test**	
PDF	**probability**	**max. distance**	**probability**	χ^2/ndf
Pythia				
CTEQ6ll	0.0000	0.0146	0.1715	1.0077
Herwig				
CTEQ6ll	1.0000	0.0000	1.0000	0.0000
CTEQ6L	0.9505	0.0012	0.0496	1.0135
CTEQ6m	0.2574	0.0023	0.2803	1.0047
MRST2004	0.9178	0.0012	0.7558	0.9973
ZEUS2005	0.1715	0.0025	0.7163	0.9994

Table A.8: Probabilities and maximum distances (resp. χ^2/ndf) for Z boson (Z sample) mass distributions using K-S test (resp. χ^2 test). The reference distributions were created from event sets generated by Herwig/Jimmy with CTEQ6ll. The number of bins is 560 000 in the range of $< 60.0 - 200.0) GeV$.

	Kolmogorov-Smirnov test		χ^2 **test**	
PDF	**probability**	**max. distance**	**probability**	χ^2/ndf
Pythia				
CTEQ6ll	0.0000	0.0146	0.0230	1.0081
Herwig				
CTEQ6ll	1.0000	0.0000	1.0000	0.0000
CTEQ6L	0.9487	0.0012	0.8414	1.0000
CTEQ6m	0.2554	0.0023	0.1771	1.0037
MRST2004	0.8903	0.0013	0.1922	1.0035
ZEUS2005	0.1645	0.0025	0.3477	1.0016

Table A.9: Probabilities and maximum distances (resp. χ^2/ndf) for lepton pair (Z sample) mass distributions using K-S test (resp. χ^2 test). The reference distributions were created from event sets generated by Herwig/Jimmy with CTEQ6ll. The number of bins is 560 in the range of $< 60.0 - 200.0) GeV$.

	Kolmogorov-Smirnov test		χ^2 **test**	
PDF	**probability**	**max. distance**	**probability**	χ^2/ndf
Pythia				
CTEQ6ll	0.0000	0.0107	0.0009	1.1963
Herwig				
CTEQ6ll	1.0000	0.0000	1.0000	0.0000
CTEQ6L	0.9980	0.0009	0.8623	0.9351
CTEQ6m	0.8649	0.0013	0.3731	1.0183
MRST2004	0.7043	0.0016	0.0224	1.1235
ZEUS2005	0.3376	0.0021	0.8117	0.9469

Table A.10: Probabilities and maximum distances (resp. χ^2/ndf) for lepton pair (Z sample) mass distributions using K-S test (resp. χ^2 test). The reference distributions were created from event sets generated by Herwig/Jimmy with CTEQ6ll. The number of bins is 5 600 in the range of $< 60.0 - 200.0)GeV$.

	Kolmogorov-Smirnov test		χ^2 **test**	
PDF	**probability**	**max. distance**	**probability**	χ^2/ndf
Pythia				
CTEQ6ll	0.0000	0.0108	0.0442	1.0345
Herwig				
CTEQ6ll	1.0000	0.0000	1.0000	0.0000
CTEQ6L	0.9875	0.0010	0.1878	1.0177
CTEQ6m	0.7639	0.0015	0.1401	1.0216
MRST2004	0.6825	0.0016	0.0005	1.0672
ZEUS2005	0.2883	0.0022	0.4099	1.0044

Table A.11: Probabilities and maximum distances (resp. χ^2/ndf) for lepton pair (Z sample) mass distributions using K-S test (resp. χ^2 test). The reference distributions were created from event sets generated by Herwig/Jimmy with CTEQ6ll. The number of bins is 56 000 in the range of $< 60.0 - 200.0)GeV$.

	Kolmogorov-Smirnov test		χ^2 **test**	
PDF	**probability**	**max. distance**	**probability**	χ^2/ndf
Pythia				
CTEQ6ll	0.0000	0.0108	0.4196	1.0016
Herwig				
CTEQ6ll	1.0000	0.0000	1.0000	0.0000
CTEQ6L	0.9815	0.0011	0.7049	1.0000
CTEQ6m	0.7501	0.0015	0.0798	1.0115
MRST2004	0.5758	0.0018	0.1484	1.0085
ZEUS2005	0.2857	0.0022	0.1396	1.0088

Table A.12: Probabilities and maximum distances (resp. χ^2/ndf) for lepton pair (Z sample) mass distributions using K-S test (resp. χ^2 test). The reference distributions were created from event sets generated by Herwig/Jimmy with CTEQ6ll. The number of bins is 560 000 in the range of $< 60.0 - 200.0) GeV$.

	Kolmogorov-Smirnov test		χ^2 **test**	
PDF	**probability**	**max. distance**	**probability**	χ^2/ndf
Pythia				
CTEQ6ll	0.0000	0.0109	0.1680	1.0036
Herwig				
CTEQ6ll	1.0000	0.0000	1.0000	0.0000
CTEQ6L	0.9791	0.0011	0.9557	0.9949
CTEQ6m	0.7408	0.0015	0.0254	1.0072
MRST2004	0.5321	0.0018	0.8549	0.9999
ZEUS2005	0.2790	0.0022	0.4115	1.0008

Appendix B

Steering parameters

```
Pythia.PythiaCommand = [
"pysubs msel 0",
"pydat1 parj 90 20000",
"pydat3 mdcy 15 1 0",
"pysubs msub 1 1",
"pysubs ckin 1 60.0",
"pydat3 mdme 174 1 0",
"pydat3 mdme 175 1 0",
"pydat3 mdme 176 1 0",
"pydat3 mdme 177 1 0",
"pydat3 mdme 178 1 0",
"pydat3 mdme 179 1 0",
"pydat3 mdme 182 1 1",
"pydat3 mdme 183 1 0",
"pydat3 mdme 184 1 0",
"pydat3 mdme 185 1 0",
"pydat3 mdme 186 1 0",
"pydat3 mdme 187 1 0"]


Jimmy.JimmyCommand = [
"iproc 11351",
"modpdf 10041",
"autpdf HWLHAPDF",
"emmin 60.",
```

"msflag 1",
"jmbug 0",
"jmueo 1",
"ptjim 4.91",
"jmrad 73 1.8",
"pltcut 0.0000000000333",
"ptmin 10.",
"prsof 0",
"rmass 198 80.425",
"rmass 199 80.425",
"rmass 200 91.19",
"gamw 2.124",
"gamz 2.495",
"taudec TAUOLA",
"clpow 1.20"]

References

[1] Francis Halzen, Alan D. Martin, Quarks and leptons:An introductory course in modern particle physics, John Wiley & Sons Inc. New York,USA, 1984

[2] J. - M. Yao et al., J. Phys. G33, 1 (2006)

[3] Jiří Hořejší, Fundamentals of Elektroweak Theory, Karolinum, Praha, 2002

[4] Jiří Chýla, Quarks, partons and Quantum Chromodynamics, *http* : $//www - hep.fzu.cz/Theory/notes/text.pdf$

[5] W.Greiner, B.Mueller, Quantum Chromodynamics, Springer-Verlag, Berlin, 2001

[6] R.K.Bock, K.Bos, S.Brandt, J.Myrheim, M.Regler, Formulae and methods in experimental data evaluation with emphasis on high energy physics, Vol. 1-3, CERN, 1984

[7] Arnold O. Allen, Probability, statistics, and queueing theory with computer science applications, Academic Press, Inc., San Diego, 1990

[8] J.Murdoch, J.A.Barnes, Statistical tables, Macmillan Press, London, 1998

[9] Harald Cramér, Mathematical methods of statistics, Princeton University Press,Princeton, 1946

[10] Ch.Arnault at al(ATLAS collaboration), The ATLAS workbook, CERN, 2006, $https : //twiki.cern.ch/twiki/bin/view/Atlas/WorkBook$

[11] ATLAS collaboration,CERN/LHCC/99-15, Detector and physics performance technical design report, Volume I

[12] ATLAS collaboration,CERN/LHCC/99-15, Detector and physics performance technical design report, Volume II

[13] George Sterman et al., Handbook of perturbative QCD, Rev. Mod. Phys., 67, 1, 157-248(1995)

[14] Jianwei Qiu, Xiaofei Zhang, Phys. Rev. D 63, 114011 (2001)

[15] Y.L.Dokshitzer, D.I.Diakonov, and S.I.Troyan, Phys. Rep. 58, 269 (1980)

[16] G.Parisi and R.Petronizio, Nucl. Phys. B154, 427 (1979)

[17] J.C.Colins, D.E.Soper, and G.Sterman, Nucl. Phys. B250, 199 (1985)

[18] G. Corcella, I.G. Knowles, G. Marchesini, S. Moretti, K. Odagiri, P. Richardson, M.H. Seymour and B.R. Webber, HERWIG 6: an event generator for Hadron Emission Reactions With Interfering Gluons (including supersymmetric processes)*, JHEP 0101 010, 1-91, 2001

[19] T. Sjoestrand, L. Loennblad, S. Mrenna, P. Skands, Pythia 6.2, Physics and Manual, hep-ph/0108264, LU TP 01-21, 2002

[20] L.W.Whitlow, E.M.Riordan, S.Dasu, S.Rock, and A.Bodek, Physics Letters B 282, 475-482 (1992)

[21] BCDMS Collaboration, Physics Letters B 223 (1989)

[22] The ZEUS Collaboration, Eur. Phys. J. C21, 443-471 (2001)

[23] The NMC Collaboration, Nuc. Phys. B 483, 3-43 (1997)

[24] Fermilab E665 Collaboration, Physical Review D 54 (1996)

[25] The H1 Collaboration, Eur. Phys. J. C 30, 1-32 (2003)

[26] The H1 Collaboration, Eur. Phys. J. C 21, 33-61 (2001)

[27] G. Corcella, I.G. Knowles, G. Marchesini, S. Moretti, K. Odagiri, P. Richardson, M.H. Seymour and B.R. Webber, HERWIG 6.5 Release Note, hep-ph/0210213, 1-7, 2002

[28] T. Sjoestrand, P. Eden, C. Friberg, L. Loennblad, G. Miu, S. Mrenna and E. Norrbin High-energy-physics event generation with Pythia 6.1, Computer Physics Commun., 135, 238, 2001

[29] W. Giele, M.R. Whalley, LHAPDF version 4.1 Users Guide, *http* : *//hepforge.cedar.ac.uk/lhapdf/manual*

[30] Ruediger Voss, CERN-PPE-92-044, 1992

[31] Davison E.Soper, Parton Distribution Functions, hep-lat/9609018

[32] Davison E. Soper, Basics of QCD perturbation theory, hep-ph/9702203 (1996)

[33] J.M.Campbell, J.W.Huston, W.J.Stirling, Hard interactions of quarks and gluons: a primer for LHC physics, Rep.Prog.Phys.70, 89-193 (2007)

[34] Drell S.D. and Yan T.M., Ann.Phys.66 578, 1971

[35] B. Webber, Ann. Rev. Nucl. Part. Sci., 36, 253-286 (1986)

[36] ATHENA, *http* : *//atlas.web.cern.ch/atlas/GROUPS/SOFTWARE/OO/architecture/*

[37] ROOT, *http* : *//root.cern.ch*

[38] *http* : *//www.itl.nist.gov/div*898*/handbook/eda/section*3*/eda*35*g.htm*

[39] *http* : *//www.itl.nist.gov/div*898*/handbook/eda/section*3*/eda*35*f.htm*

[40] *http* : *//en.wikipedia.org/wiki/Chi* − *square_goodness* − *of* − *fit_test*

[41] *http* : *//en.wikipedia.org/wiki/Kolmogorov_test*

[42] *http* : *//root.cern.ch/root/html/TH*1*.html#TH*1 : *KolmogorovTest*

[43] *http* : *//root.cern.ch/root/html/TH*1*.html#TH*1 : *Chi*2*Test*

[44] *http* : *//atlas.ch/atlas_photos/fulldetector/fulldetector/ATLAS_Silver_White_MK.jpg*

[45] *http* : *//atlas.ch/atlas_photos/liqargcal/liqargcal_general/LAC_general-view.gif*